2016

Lead Free CH3NH3SNI3 Perovskite Thin-Film with P-type Semiconducting Nature and Metal-like Conductivity

Anastasiia Iefanova
South Dakota State University

LEAD FREE CH3NH3SNI3 PEROVSKITE THIN-FILM WITH P-TYPE SEMICONDUCTING NATURE AND METAL-LIKE CONDUCTIVITY

BY

ANASTASIIA IEFANOVA

A dissertation submitted in partial fulfillment of the requirements for the

Doctor of Philosophy

Major in Electrical Engineering

South Dakota State University

2016

LEAD FREE CH3NH3SNI3 PEROVSKITE THIN-FILM WITH P-TYPE SEMICONDUCTING NATURE AND METAL-LIKE CONDUCTIVITY

This dissertation is approved as a creditable and independent investigation by a candidate for the Doctor of Philosophy in Electrical Engineering degree and is acceptable for meeting the thesis requirements for this degree. Acceptance of this dissertation does not imply that the conclusions reached by the candidate are necessarily the conclusions of the major department.

Dr. Qiquan Qiao — Date
Dissertation Advisor
Graduate Coordinator/
Harold. C. Hohbach Associate Professor

Dr. Steven Hietpas — Date
Head, Electrical Engineering
and Computer Science

Dean, Graduate School — Date

ACKNOWLEDGEMENTS

I want to thank Dr. Qiquan Qiao, my dissertation advisor, for significant support of my research work that has an outcome in this thesis. I admire him for his guidance and advice. I am also grateful to Dr. David Galipeau, Dr. Yung Huh, Dr. Hyeun Joong Yoon, and Dr. Heidi Mennenga for being my committee members. Similarly, I want to acknowledge graduate students Ashish Dubey, Nirmal Adhikari, Devendra Khatiwada for their fabrication characterization help.

I appreciate the financial support from the National Science Foundation Major Research Instrumentation (MRI) program grant 1428992, National Science Foundation Experimental Program to Stimulate Competitive Research program grant 0903804 and by the State of South Dakota.

CONTENTS

ABBREVIATIONS

AC alternating current

AFM atomic force microscope

AM air mass

CE counter electrode

CS-AFM current sensing atomic force microscopy

CPD contact potential difference

DC direct current

DI de-ionized

DMF dimethylformamide

DMS dimethyl sulfoxide

DSSC dye sensitized solar cell

ETL electron transport layer

FTO fluorine tin oxide

FWHM full width half maximum

GB grain boundary

GBL gamma butyrolactone

HTL hole transport layer

IPA isopropanol

ITO indium tin oxide

IPCE incident photon to current efficiency

KPAFM kelvin probe atomic force microscopy

NIR near infrared

NREL National Renewable Laboratory

PV photovoltaic

SC semiconductor

SCLC space charge limited current

SEM scanning electron microscope

SMU source/monitor unit

STC standard test conditions

TBP tert-Butylpyridine

TCO transparent conductive oxide

UV ultraviolet

VIS visible

Xe xenon

XRD X-ray diffraction

LIST OF FIGURES AND TABLES

ABSTRACT

LEAD FREE $CH_3NH_3SNI_3$ PEROVSKITE THIN-FILM WITH P-TYPE SEMICONDUCTING NATURE AND METAL-LIKE CONDUCTIVITY

ANASTASIIA IEFANOVA

2016

$CH_3NH_3SnI_3$ and $CH_3NH_3PbI_3$ have become very promising light absorbing materials for photovoltaic devices over the last several years. $CH_3NH_3PbI_3$ based perovskite solar cells have reached a solar-to-electricity conversion efficiency of ~ 22%. Nevertheless, $CH_3NH_3PbI_3$ perovskite solar cells contain lead, which has serious consequences for the environment and human health. In this work, the lead was replaced with less toxic tin. Lead free $CH_3NH_3SnI_3$ perovskite thin film was prepared by two low temperature solution processing methods and characterized using various tools such as X-ray Diffraction (XRD) and absorption spectroscopy (UV-VIS). The distinctive p-type semiconducting nature and metal like conductivity of $CH_3NH_3SnI_3$ were confirmed by the measurements of electrical and optical properties. Crystal structures and uniform film formation of $CH_3NH_3SnI_3$ layer were analyzed by XRD and scanning electron microscopy (SEM). The $CH_3NH_3SnI_3$ film morphology, uniformity, light absorption and electrical properties strongly depend on the preparation methods and precursor solutions. The $CH_3NH_3SnI_3$ perovskites fabricated using dimethylformamide (DMF) exhibited higher crystallinity and stronger light harvesting capability than those fabricated using a blend solvent of dimethyl sulfoxide (DMSO) and gamma-butyrolactone (GBL). The local

nanoscale photocurrent mapping confirmed that $CH_3NH_3SnI_3$ can be used as an active layer and has a potential to fabricate lead free photovoltaic devices. The $CH_3NH_3SnI_3$ film also showed a strong absorption in visible and near infrared spectrum with an absorption onset of 1.3 eV.

CHAPTER 1. INTRODUCTION

1.1 Background

The rapidly growing global energy consumption cannot be met by limited supplies of fossil fuels in the future [1]. The main concern about fossil-based fuels is their impact on the environment provoking catastrophic climate change. The carbon released into the atmosphere from burning fuels combines with oxygen in air to form carbon dioxide (CO_2) – one of the green-house gases in earth's atmosphere. Burning one gallon of petroleum releases approximately 19.64 pounds of carbon dioxide [2]. Excessive green-house gas emissions caused by the consumption of fossil-based fuels and a possible global energy crisis due to the limited resources are significant motivators in the efforts to replace traditional fuels with nonpolluting renewable energy sources similar to hydro energy, energy of wind, biofuels, and solar energy.

Renewable energy based on the solar power is a very attractive and promising technology as it does not yield any air pollution or hazardous waste, and it does not require any consumption of liquid or gaseous fuels. Since sunlight is an omnipresent form of energy, it enables the development of geographically diverse photovoltaic (PV) systems that are immune to international energy politics and unstable fossil-fuel-based market [3-6].

Obviously, energy required to make photovoltaic systems has to be a small fraction of the total energy produced during their lifetime. In spite of the fact that the sun delivers in one hour enough energy to supply world's annual energy consumption needs [1], solar photovoltaics have not become a dominant energy supplier in the energy market. This is because solar energy has not been cost-competitive with traditional energy sources. Nevertheless, due to the gradual decline of production cost of PV cells and constant increase

in the price of fossil-based fuels, the solar photovoltaics will become a cost-competitive in near future, opening enormous possibilities in the renewable energy market [7].

The major problems in producing electricity by solar panels is their rather low efficiency and high cost for the large area photovoltaics. The theoretical maximum efficiency (the so-called Shockley-Queisser limit under the standard AM1.5 solar mass) for a single-junction monocrystalline silicon cell is 32.9% [8]. Considering additional practical energy losses in the cell including junction loss, contact loss, recombination loss and near bandgap absorption losses, the maximum efficiency of a for silicon solar cells gets capped at about 25 % [9]. In addition, they are not economical when compared to grid based energy supply due to their high cost of raw materials and production. Crystalline silicone solar cells require high purity silicon as starting material and further need several sophisticated vacuum processing steps for fabrication. Silicon solar cells also require high temperature processing and are brittle limiting their application to flexible solar cells [10].

Today's solar cell production technology is categorized as mono- and polycrystalline silicon cells with typical efficiencies for commercially available modules of ≈16% [11, 12], thin-film cells similar to $CuInSe_2$, $CuInGaSe_2$, CdTe, and film amorphous silicon with typical energy conversion efficiencies in range of 10 – 12% [11, 13]. Photovoltaic technologies have also matured to the stage of elaboration and implementation of the 3rd generation solar cells based on "high performance and low cost" products. These products are made of novel materials that allow to reduce energy losses in the cell due to the application of nanotechnology including nanostructures (quantum wells, wires, dots [14] , spectrum-shifting cells[15], and use of plasma effects [16]), quasi-crystalline and even amorphous materials made out of monodispersed colloids, polymers, gels, and electrolytes. Solar cells

that utilize organic materials as the active light absorbers such as polymer organic bulk heterojunctions and dye-sensitization are also referred to as 3rd generation PV devices. These solar cells are projected to deliver solar electric power at very low costs (0.1-0.5 $US/Watt) [12]. Over the last two decades, different solution processed organic and hybrid organic-inorganic solar cells [17] have been passionately studied. Nevertheless, the efficiencies of those type of cells required to compete in the energy market have not yet been realized. The goal of the solar industry is to produce low-cost PV modules that are highly efficient compared to other energy sources.

Figure 1. 1 shows the highest reported efficiency trends for different types of solar cells fabricated in research laboratories compiled and plotted by National Renewable Energy Laboratory (NREL) from 1975 to 2015. Different types of solar cells include but not limited to multijunction, single junction GaAs, crystalline silicon, thin film solar cells (CIGS and CdTe), quantum dot, dye sensitized solar cells (DSSCs)[18, 19], and organic polymer solar cells [20-26]. Some of the notable efficiencies are 24.7% for mono-crystalline Si solar cells, 44.4% for multi-junction InGaAs/GaAs/InGaP reported by Sharp technologies, 20.4% for CdTe solar cells reported by First Solar, 11.9% for DSSCs and 10.6% for tandem polymer solar cells. In recent years, starting from 2009 perovskite solar cells [27-31] have been gained significant attention in photovoltaic application by reason of their high efficiencies and low-cost fabrication. Their efficiency dramatically increased from 9.7% [32] up to 19.3 % [33]. The advent of perovskite semiconductors could be the

key to reaching this goal of making inexpensive devices that are highly efficient at converting sunlight into electricity.

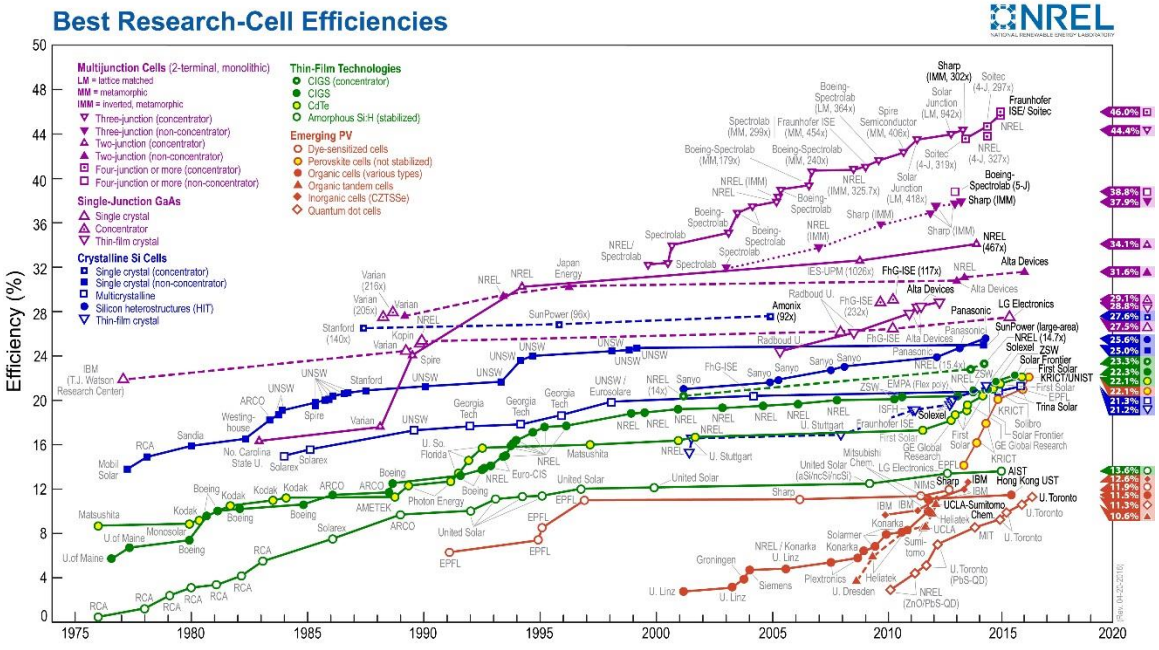

Figure 1. 1 NREL`s latest chart of best research-cell efficiencies (nrel.gov).

Perovskite solar cells offer several other advantages over conventional inorganic counterparts. This light absorbing material has strong light absorption (1.5×10^4 cm^{-1}) and diffusion lengths larger than 1 μm for both electrons and holes [34, 35]. In addition, this material can transport both positive and negative charges [36].

It is remarkable that the open circuit voltage of the perovskite solar cells can reach up to more than 1 V [37], compared 0.7 V for typical silicon solar cells. According to Figure 1. 1, perovskite solar cells reached more than 20% efficiency in few years [38]. Even though the efficiency maximum of perovskite soar cells still remains uncertain, it appears that the efficiency will continue to raise. Moreover, perovskite solar cells have been fabricated using

variety of preparation techniques, different precursor solutions, and different morphologies [39].

The toxicity of lead is one of the biggest issues with this material. Lead based composition has potential to inflict harm upon both the human body and the natural environment [40, 41]. The perovskite compounds are salt-like minerals that can easily be dissolved in water or water vapor. The chance of dissolved lead slats leaking into rivers and onto the rooftops of homeowners is an obstacle to bring this technology to the market. Since lead has very bad consequences to the human health and the environment in general, it is highly desirable for lead to be replaced with other non-toxic elements. The most feasible substitutes for lead (Pb) in the perovskite materials are tin (Sn) and germanium (Ge) that also belong to the group 14 metals in the periodic table [42]. Nevertheless, the stability issue associated with the 2^+ oxidation state becoming more dominant when going up in the group 14 elements of the periodic table, meaning that when using Sn and Ge to replace Pb in perovskite structure, the chemical instability becomes a significant problem [43].

The conducting halide $CH_3NH_3SnI_3$ perovskite compound is known as a low carrier density p-type metal [44]. It was reported that charge transport in $CH_3NH_3SnI_3$ perovskite arises with a low hole carrier concentration. The metallic properties of this compound results from unprompted hole doping during the crystallization process, instead of the electronic structure of the material [45]. In the $CH_3NH_3SnI_3$ perovskites, there is a facile tendency to behave as a p-type semiconductor showing metal-like conductivity. However, the $CH_3NH_3SnI_3$ compound can perform as a n-type semiconductor depending on preparation methods [46]. Another study suggested that the hole and electron mobility can

be actually superior in $CH_3NH_3SnI_3$ perovskites and can be considered as more efficient semiconductors in terms of charge transport characteristics compared to their lead based counterparts [47-49]. $CH_3NH_3SnI_3$ perovskites, specially, have demonstrated excellent mobility when used in transistors [50]. However they can also be doped purposefully or inadvertently to be converted into metallic [44, 45].

The $CH_3NH_3SnI_3$ perovskite has an optical band gap of 1.3 eV, indicating a significant red shift compared with the benchmark light-harvesting material $CH_3NH_3SnI_3$, whose optical band gap is ~1.55 eV [51]. It was reported that $CH_3NH_3SnI_3$ analogue could serve as a lead-free light absorbing material. The reported efficiencies of 5-6% of lead-free devices using $CH_3NH_3SnI_3$ as a light absorber has demonstrated the potential [43, 52]. Despite prosperous applications of the $CH_3NH_3SnI_3$ perovskite compound in photovoltaics, a systematic understanding of its electronic, optical, and electric properties is essential for further optimizing material properties.

Even though there have been previous attempts to fabricate lead free perovskite solar cells [43, 52], there is a wide range in the efficiency of the $CH_3NH_3SnI_3$ solar cells [52]. The properties of $CH_3NH_3SnI_3$ still remain uncertain. Some reports explain cubic structure of $CH_3NH_3SnI_3$ [43] whereas others describe tetrahedral structure [52]. The charge transport properties of $CH_3NH_3SnI_3$ are also debatable. Some calculations predict $CH_3NH_3SnI_3$ to be better electron transport material compared to $CH_3NH_3Pb_3$ [48], while other papers describe $CH_3NH_3SnI_3$ as a hole transporter [46]. Sn perovskites crystallize directly upon spin-coating, which is actually impediment to form uniform film coverage leading to poor photovoltaic device efficiency. Insufficient coverage of perovskite film may result in shunt paths between hole transport layer and compact TiO_2, which can

perform as a parallel diode in solar cell, reducing open circuit voltage and the fill factor. The considerably low efficiency of lead-free $CH_3NH_3SnI_3$ perovskite solar cells can also be due to oxidation of Sn^{2+} into the formation of Sn^{4+} in ambient air or the presence of oxygen. Chemical instability of $CH_3NH_3SnI_3$ in ambient air makes it challenging to perform material characterization measurements. $CH_3NH_3SnI_3$ degrades rapidly and oxidizes in air that leads to the formation of oxides and hydroxides of tin and methylammonium iodide. Systematic analysis of electronic, optical, and structural properties of $CH_3NH_3SnI_3$ is needed to better understand the nature of $CH_3NH_3SnI_3$ to understand the limits of the material and suppress its oxidation processes in order to make stable and high performance lead free perovskite solar cells.

In the field of photovoltaic, the selection of material is a trade-off between cost, efficiency, and stability. Strong and broad optical absorption, fast charge carrier transport and separation, low recombination rate are requirements for an ideal solar cell material [53]. Investigation the properties of solar cell material and controlling its properties through advances engineering can lead to the fabrication of efficient and cost effective photovoltaic devices. In order to fabricate more efficient lead free perovskite solar cells, the optoelectrical, electronic, and structural properties of lead free $CH_3NH_3SnI_3$ materials are needed to be investigated.

In this work, an analytical study of optical and electrical properties of $CH_3NH_3SnI_3$ films based on different solvents such as dimethylformamide (DMF) and combination of dimethyl sulfoxide (DMSO) with gamma-butyrolactone (GBL) was presented in this work. X-ray diffraction (XRD) spectra, optical and morphological properties of $CH_3NH_3SnI_3$ film was conducted and correlated them with electrical properties using current-sensing

atomic force microscopy (CS-AFM). It was found that $CH_3NH_3SnI_3$ is a semiconductor with metallic behavior. Moreover, the photocurrent is mostly distributed within grain boundaries whereas dark current is within the interior of grains. To pinpoint the differences and similarities between lead based $CN_3NH_3PbI_3$ films and tin based $CH_3NH_3SnI_3$ counterparts, the comparative study was performed in terms of stability, morphological, and electrical properties of both thin films.

1.2 Previous work

Perovskite solar cells are constructed of organic-inorganic semiconductor material with a perovskite polycrystalline structure. A typical chemical composition of lead based perovskites is $CH_3NH_3PbX_3$, where X is a halide atom (I, Cl, Br, or a combination of some of them).

In 2009, $CH_3NH_3PbI_3$ and $CH_3NH_3PbBr_3$ perovskites were first used as a light absorbing material in dye-sensitized solar cells by Miyasaka et al. [32] with the efficiency for bromide and iodide of 3.8% and 3.1%, respectively. The efficiencies were much lower than the expected ones. The perovskite layers were washed away by liquid electrolyte after few minutes. However, the theoretical photocurrent densities were higher than the measured ones. The drawback of this DSSC based perovskite cell structure was the instability of the $CH_3NH_3PbI_3$ due to liquid electrolyte. Surface protection of the deposited $CH_3NH_3PbI_3$ is thus to needed to be developed to increase the stability of the device. The band gap of lead bromide was estimated about 2.25 eV, whereas the band gap of lead iodide perovskite was estimated around 1.55 eV. The estimated band gap values were extracted

from the threshold values in the incident photon-to-current conversion efficiency (IPCE) spectra.

In 2012, the liquid electrolyte was changed to solid hole transport material called Spiro-OMeTAD by Kim et al. The power conversion efficiency exhibited 9.7% along with remarkable long-term stability. The thickness of TiO_2 layer was ~ 0.5 μm for improved device performance [34]. The electronic band alignment between absorbing layer and hole transport layer, and electron transport layer was discussed as well [54]. Nevertheless, the uncontrolled crystallization of the perovskite resulted in wide morphological variations during spin-coating deposition process, which can lead to variations of the device performance and limiting the prospects of practical applications.

In 2013, the efficiency of perovskite ($CH_3NH_3PbI_3$) lead-based cell reached of up to 15 % by Burschka et al. [37]. The issue of uncontrolled precipitation of perovskite layer was solved by sequential (two-step) solution deposition process for the formation of the perovskite absorbing layer within the porous TiO_2. Primary, PbI_2 solution was deposited on nonporous titanium dioxide film. Then, the perovskite pigment was formed by exposing the samples into $CH_3NH_3I_3$ solution. This fabrication method allowed more précised control of perovskite morphology resulting in the increase of reproducibility of the device performance.

In 2012, the performance efficiency of 10.9% of perovskite ($CH_3NH_3PbI_2Cl$) lead-based cell as a single-junction solar cell under simulated sunlight by Lee et al [55]. Solid spiro-MeOTAD was used as hole transport layer and mesoporous alumina as an electron transporter layer for better electron transport through the device. This mesostructured solar

cell exhibited of more than 1.1 V of open circuit voltage, which is higher than typical silicon solar cells.

In 2014, with the incorporation of interface engineering, Yang group reported a 19.3% of power efficiency in lead based perovskite solar cells [33]. The formation of perovskite layer was performed from solutions at low temperatures and humidity controlled environment that lead to substantially decreased carrier recombination. The fabrication procedure was performed at low temperature (<150°C). The electron transport channel was also improved by modifying the ITO electrode to reduce its work function and by doping TiO_2 to increase its carrier concentration. The perovskite solar cells were fabricated with a device configuration analogous to the typically used planar device structure with some modifications.

Recently, as certified by National Renewable Energy Laboratory [56], 20.1± 0.4% power conversion efficiency of perovskite has been reached. Their power efficiency outperform other solar cells based on DSCs, CdTe and polymer solar cells [57-59]. The improved efficiency was achieved by controlling the thickness of perovskite absorbing layer and electron transport layer (ETL) as well by their interfaces. More study has been done to find the best device structure in terms of robustness and stability. It was showed that perovskite solar cells can be made in both planar and bulk heterointerface structures with high performance. However, all the above reported perovskite solar cell uses contain toxic lead in the form of salts, which is very harmful for environment and human body.

In 1995, the transport, optical, and magnetic properties of $CH_3NH_3SnI_3$ were tested over the temperature range from 1.8 K to 300 K by Mitzi et al [32]. It was investigated that this conducting halide perovskite behaves as a low carrier density p-type metal. A free carrier

infrared reflectivity spectrum was observed at 1600 cm^{-1} indicating the metallic nature of this compound.

In 2013, phase transitions, photoluminescence properties, and hall effect of $CH_3NH_3SnI_3$ and $CH_3NH_3PbI_3$ were studied by Stoumpos et al. [46] It was investigated that physical and chemical properties of $CH_3NH_3SnI_3$ and $CH_3NH_3PbI_3$ intensely depend on the preparation process. It was also observed that $CH_3NH_3SnI_3$ compound can behave as n-type semiconductor with low carrier concentration if prepared from solution. Due to the tendency of Sn^{2+} towards oxidation through solid state reactions in ambient air or the presence of oxygen, $CH_3NH_3SnI_3$ perovskite compound can be self-doped with Sn^{4+}. The self-doping of $CH_3NH_3SnI_3$ perovskite compound with Sn^{4+}can cause the material behave as a p-type semiconductor exhibiting metal-like conductivity. However, the compounds were studied in the form of powder rather than thin films, which is crucial for photovoltaic application.

In 2014, modeling of electronic, optical, and transport properties and relativistic GW of $CH_3NH_3SnI_3$ and $CH_3NH_3PbI_3$ were studied by Umari et al [48]. To point the differences and similarities of these two perovskite compounds, a number of calculations using Density Functional Theory and developed GW method incorporating spin-orbit coupling were carried out. This allowed to precisely model the optical, electronic, and charge transport properties of $CH_3NH_3SnI_3$ and $CH_3NH_3PbI_3$ materials. It was found out that $CH_3NH_3SnI_3$ has a metallic nature and can be predicted to be better electron transport layer than $CH_3NH_3PbI_3$ due to the different weight of relativistic effects in tin- and lead-based perovskite materials.

In 2014, it was an attempt to make lead-free perovskite cell with tin iodide ($CH_3NH_3SnI_{3-x}Br_x$) by Hao et al [43]. The performance efficiency of lead-free perovskite

solar cells was 5.73%. The absorption onset was measured at 950 nm, indicating a significant redshift compared to the $CH_3NH_3PbI_3$ counterpart. Additional efficiency improvements were predicted if a better understanding of the charge carrier dynamics and interfacial engineering are implemented. The fabricated cells showed stability issues due to Sn^{2+} oxidation in ambient air. The indication of the solar cell degradation was the change of color happened almost immediately after the samples were taken out of the nitrogen glovebox. Uneven $CH_3NH_3SnI_{3-x}Br_x$ film coverage can also be a reason for poor efficiency. Insufficient coverage of perovskite film may result in shunt paths between hole transport layer and compact TiO_2 layer. This means that the fabrication procedure needs to be improved and controlled in resized manner.

In 2014, the efficiency of tin-based ($CH_3NH_3SnI_3$) perovskite cell reached 6 % by Noel et al [52]. The precursor solution of $CH_3NH_3SnI_3$ perovskite was based on DMF solvent. The device architecture was similar to previous work. The device was completely lead free. Nevertheless, the reproduction of the results was still low due to not uniform $CH_3NH_3SnI_3$ film coverage and difficulty to control the morphology during the crystallization process of $CH_3NH_3SnI_3$. Spiro-OMETAD was used as a hole transporter layer including tert-Butylpyridine (TBP) and Li salts as doping, which was harsh on active $CH_3NH_3SnI_3$ film. This resulted in $CH_3NH_3SnI_3$ film degradation. The color change $CH_3NH_3SnI_3$ film from bark-brown to white upon deposition of spiro-OMETAD was an indication of film degradation. It also should be mentioned that some $CH_3NH_3SnI_3$ devices fabricated with DMF as a precursor solution exhibited short-circuit behavior. This behavior can be also attributed to the film defects and voids formed during the spin-coating.

In 2015, the problem of short-circuit behavior was solved by Hao et al. fabricating of highly uniform and pinhole-free $CH_3NH_3SnI_3$ perovskite film by controlled crystallization process [60]. The improved $CH_3NH_3SnI_3$ film morphology was achieved using DMSO solvent for precursor solution. The fabricated and tested lead free $CH_3NH_3SnI_3$ solar cell was based on mesoporous TiO_2 layer but in the absence of hole transporting material. The efficiency of fabricated lead free $CH_3NH_3SnI_3$ device was as low as 3.15% with low 320 mV open circuit voltage and low fill factor of 0.49.

In summary, although there have been earlier attempts to fabricate lead free perovskite solar cells and investigate their material properties, their electrical and optical properties still remain uncertain. The understanding of correlation between morphological and electrical properties is opening the way to the design of lead free perovskite solar cells. The importance of this work is to understand and control the electrical properties of Sn-based perovskite materials that can lead to the fabrication of efficient, stable, and environmentally safe lead free perovskite solar cells.

1.3 Motivation

There is a strong need to understand electrical, optical, and structural properties of $CH_3NH_3SnI_3$ perovskite material in order to fabricate stable and high performance lead free perovskite solar cells.

1.4 Objectives

The objectives of this dissertation were to understand electrical, optical, and structural properties of $CH_3NH_3SnI_3$ films and fabricate high performance lead free perovskite solar cells. This was the first report on the understanding of morphological,

electrical, and optical properties of $CH_3NH_3SnI_3$ perovskite materials and the correlation between the morphology and light harvesting properties that can lead to improved charge transport.

The tasks of this dissertation were to:

- Establish fabrication procedure of lead-free $CH_3NH_3SnI_3$ perovskite thin film using different solution process techniques
- Characterize $CH_3NH_3SnI_3$ perovskite thin film using SEM, AFM, UV-VIS, XRD to improve the quality of the film
- Correlate morphological and electrical properties of $CH_3NH_3SnI_3$ perovskite thin film using CS-AFM
- Perform comparative study of morphological and electrical properties of tin based and lead based perovskite materials
- Analyze stability properties of $CH_3NH_3SnI_3$ perovskite thin film

CHAPTER 2. THEORY

This chapter describes the theory of perovskite solar cells and mechanisms of charge transport. The theory behind the characterization techniques utilized in this dissertation is also presented.

2.1 Power conversion efficiency of photovoltaic devices

The overall sunlight-to-electric-power conversion efficiency, η, of photovoltaic device is the ratio between the maximum attainable electric power, P_{max}, at the solar cell electrodes to the input optical power, P_{in}, in Watts incident to the solar cell given by:

$$\boldsymbol{\eta = \frac{P_{max}}{P_{in}} = \frac{V_{oc} \cdot I_{sc} \cdot FF}{P_{in}}} \tag{2.1}$$

where

$$\boldsymbol{P_{max} = V_{max} \cdot I_{max}} \tag{2.2}$$

Where I_{max}, the maximum photocurrent, and V_{max}, maximum voltage, are obtained at the maximum power point of a typical photovoltaic device. A typical cell response with I_{max}, V_{max}, and P_{max} is shown in Figure 2.1.

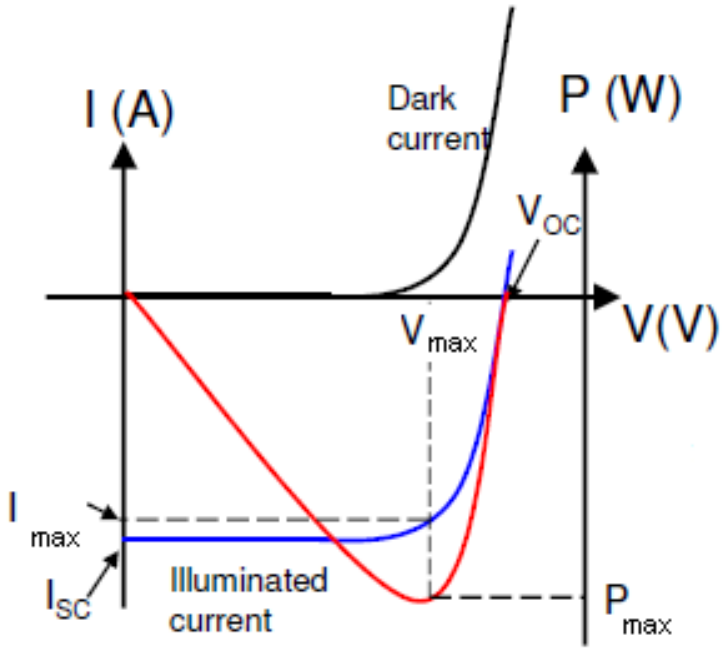

Figure 2.1 Current-voltage and power-voltage curves.

The fill factor, *FF*, the squareness of the IV characteristics of solar cells is defined as:

$$\boldsymbol{FF} = \frac{\boldsymbol{P_{max}}}{\boldsymbol{V_{oc} \cdot I_{sc}}} \tag{2.3}$$

Where V_{oc} is the voltage developed across a cell if the two terminals of the device are open. I_{sc} is short circuit current delivered by the solar cells device if the value of the load resistance is zero, or if the two terminals of the device are shorted to each other. In open circuit conditions, the photocurrent does not flow through the load; it is redirected through the internal diode. For variety of solar cells, the V_{oc} can be calculated by:

$$\boldsymbol{V_{oc}} = \frac{\boldsymbol{k \cdot T}}{\boldsymbol{q}} \boldsymbol{\ln}\left(\frac{\boldsymbol{I_{sc}}}{\boldsymbol{I_0}} + \boldsymbol{1}\right) \tag{2.4}$$

where q is the charge of electron, T is temperature, k is Boltzmann constant, and I_0 is the dark saturation current of the diode. At the voltage range is between 0 and V_{oc}, the photovoltaic device generates power. When the voltage is $V<0$, the illuminated solar cell consumes power to produce a photocurrent. The diode in this regime operates as a photodetector where its current is linearly sensitive to light intensity and is its value bias independent. At $V>V_{oc}$, the dark current through the diode is larger than the photocurrent developed by the cell hence the solar cell sinks current from the external source. In this regime, the device start to consume power and operates like a light emitting diode, particularly if the solar cell is made of a direct bandgap semiconductor [61].

The efficiency of photovoltaic cell is often expressed in term of short circuit current density, J_{sc}, as:

$$\boldsymbol{J_{sc} = I_{sc}/A} \tag{2.5}$$

where A is the active area of the solar cell. Then, the power conversion efficiency, η, of the photovoltaic device can be expressed as:

$$\boldsymbol{\eta = \frac{FF \cdot V_{oc} \cdot J_{sc}}{P_{op}}} \tag{2.6}$$

where P_{op} is the optical power density incident to the device in W/cm^2. Under the Standard Test Condition (STC), the solar cell efficiency is measured by an AM 1.5 compatible light with incident power density of 1000 W/m^2 equivalent to 100 mW/cm^2 at a temperature of 25 ^{o}C.

2.2 Operation principle of perovskite solar cells and charge transfer kinetics in perovskite solar cells

The term perovskite is derived from crystal structure with the general stoichiometry as ABX_3, where A is an organic cation, B a divalent metal ion, and X an anion (O^{2-}, Cl^-, Br^-, I^-, or, in a few instances, S^{2-}), respectively, that bonds to both as shown in Figure 2.2. The perovskite crystal structure is arranged into octahedral symmetry. The idealized perovskite structure is cubic, where A cations occupy 12 coordinates. B cations are placed in octahedral spaces surrounded by the X anions [62].

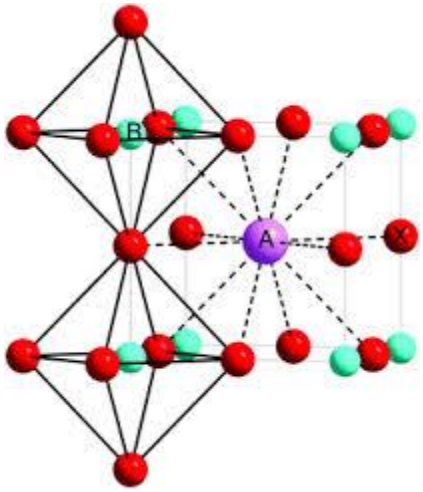

Figure 2.2 Perovskite crystal structure [63].

There are many various materials that have perovskite crystal structure similar to calcium titanate ($CaTiO_3$), strontium titanate ($SrFeO_3$), magnesium carbonate ($MgSiO_3$), barium titanate ($BaTiO_3$), strontium zirconium oxide ($SrZrO_3$), lithium niobate ($LiNbO_3$), and the nonoxide $KMgF_3$, that can form a broad range of materials, including dielectrics [64, 65], semiconductors [46], superconductors [66, 67], ferroelectrics [68, 69], magnetic and ionic conductors [70]. In a perovskite structure, the substitute of A inorganic cations

with another suitable organic cation is the fundamental to a wide range of properties [71]. With the replacement of A cations with a proper organic cationic molecule, B ion with an inorganic metal in group 14 of periodic table, and X with halides, the perovskites structure can exhibit photovoltaic properties [32, 72] as well as used in thin-film transistors [73], and light-emitting diodes[72, 73].

Organo-metal halide perovskites are tightened with hydrogen bonds between the halide and amino group ions. However, the bonds among the organic ions are weak and have Vander Waals nature. The divalent transition metal ions that belong to group 14 of periodic table (including Sn^{2+} and Pb^{2+}) have a potential for low-temperature device fabrication and good optoelectronic properties [42, 70, 74].

The bandgap of organo-metal halide perovskites can be degreased by lowering the Pauling electronegativity between the metal cation and halide anion. The optical absorption can be enhanced by the replacement of single halides with mixed halides with different ratios[75].

The geometrical size of organic cations is critical to make fit into perovskite structure. Thus for A cations, the best fit is the smallest organic molecules such as methylammonium ions ($CH_3NH_3I^+$). Nonetheless, the small A cations' size must be compensated by tightening the contact with anions in the cubic structure, which tends to distort the octahedral BX_6 structure and introduces the distortion factor. This distortion factor is called Goldschmidt's tolerance factor [76]. The Goldschmidt's tolerance factor (t) is described as [77]:

$$t = \frac{(R_A + R_X)}{\sqrt{2}(R_B + R_X)}, \tag{2.7}$$

where R_A, R_B, and R_X are the corresponding ionic radii of A, B, and X. Since the radius of Pb^{2+} metal cation (R_B = 1.19 A) is larger than that of Sn^{2+} metal cation (R_B = 0.93 A) [78], it is evident that the lead based perovskites have lower distortion factor than their tin based counterparts, meaning higher structure tolerations.

The ferroelectric nature of organo-metal halide perovskites is due to polar nature and permanent dipole moment of $CH_3NH_3I^+$ ions, as well as structural distortions of metal halide anions carried by the ion pairs of lead (6s2) and tin (5s2).

Methylammonium ions have permanent dipole moment and insulator nature whereas iodine ions exhibit semiconducting properties. The semiconductor metal iodide are places between methylammonium ions, thus can freely change their orientation and produce the octahedral dielectric confinement of excitons [79]. Due to organic and inorganic nature of perovskite structure, the excitons exhibit lower binding energies and higher Bohr's exciton radius [80]. These properties result into better charge transport. In addition, strong polarization of methylammonium ions due to permanent dipole moment, presence of inorganic anions and organic cations lead to higher dielectric constants and excellent charge transport [67].

The charge transport in organo-metal halide perovskite solar cells generally is similar to the conventional dye-sensitized solar cells. Figure 2.3 shows the basic architecture of a perovskite solar cell. The photoanode is composed of a thin mesoporous semiconducting layer (typically (TiO_2, Al_2O_3, etc.)) deposited on transparent conducting oxide glass substrate and coated with a layer of perovskite material. The transparent conducting oxide (TCO) films, such as indium tin oxide (ITO) and fluorine- doped tin oxide (FTO), are commonly utilized because of their high optical transmittance, high

photoconductivity, and low electrical resistance [81]. Though, FTOs produce higher efficiencies compared to ITOs due to their high thermal stability.

The role of perovskite material is to absorb the light, generate excited photoelectrons and to inject of the excited electrons into the TiO_2. The mesoporous TiO_2 layer provides a pathway for the injected electrons to move from perovskite layer to the transparent conducting substrate. The perovskite layer is sandwiched between the electron transport layer and hole transport layer, which is typically poly(3-hexylthiopene-2,5-diyl (P3HT) or spiro-OMeTAD. A hole transport layer is necessary for charge separation and hole transport from counter electrode. The counter electrode composed of silver (or another metal) deposited onto the hole transport layer by thermal evaporation.

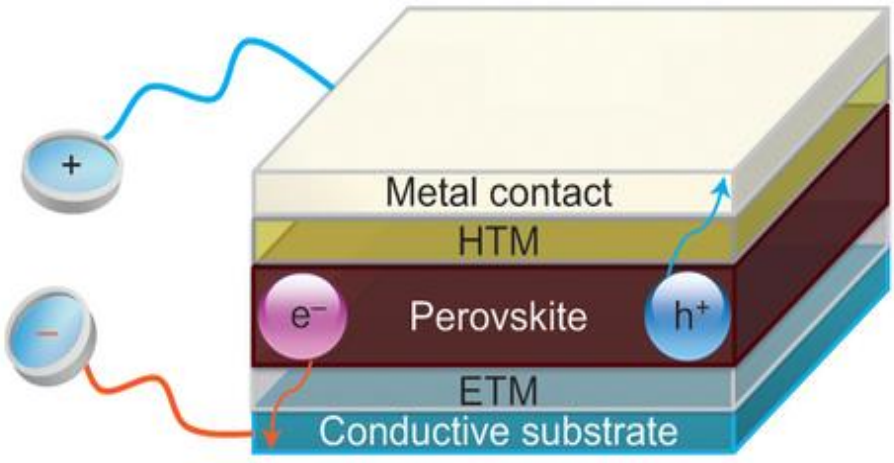

Figure 2.3 A schematic representation of a perovskite solar cell [82].

Figure 2.4 describes the energy band structure of a typical perovskite solar cell. Light is absorbed by the perovskite layer. Electrons and holes are then generated. The

electrons are injected into an electron transport layer whereas holes are injected into a hole transport layer. The injected electrons move towards the photo-electrode surface through the TiO_2 particles and create electrical current. However, low intrinsic mobility of TiO_2 results in the unbalanced charge transport. This is the reason that TiO_2 was replaced with other electron transport materials such as Al_2O_3 [83]. Then, the extraction of those charge carriers to the external circuit is made by TCO and counter electrode contacts. The photocurrent of perovskite solar cells depends on the incident light intensity, the efficiency of charge injection in the excited state, the recombination rate of electrons and holes, and the efficiency of charge transport in the conduction band of TiO_2 to the counter electrode. The open circuit voltage in perovskite solar cells is the energy gap between the conduction band of TiO_2 layer and the fermi level of hole transport layer [84].

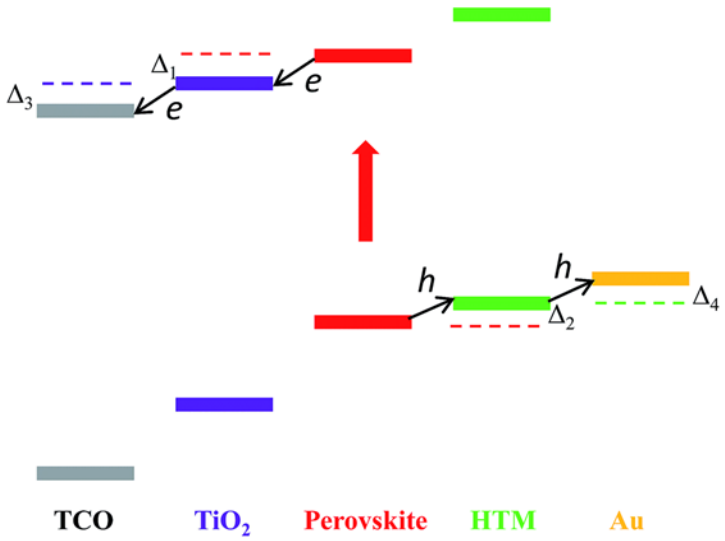

Figure 2.4 The energy band structure of a typical perovskite solar cell [42].

Based on the above discussion, the performance of perovskite solar cells depends on various factors including but not limited to film structure, surface morphology, porosity

of the layer, grain sizes, particle size of semiconducting (TiO_2) layer, absorption coefficient, crystal size of perovskite material, electron transport process and recombination rates.

2.3 Characterization techniques of Perovskite thin films

2.3.1 X-ray Diffraction Spectroscopy

The distances between atoms in crystal structures is nearly equals to the wavelength of X-rays. X-ray diffraction is a scattering of enhanced beams by spaced atoms in some directions. By phase relationship between beams of elastically scattered X-rays, the beam interference can be constructive and destructive. If the path length difference is equal to an integer multiple of the wavelength of the X-ray beam, the interference is constructive As shown in Figure 2.5 the path difference X-rays scattered from panels 1 and 2:

$$\overline{OA} + \overline{OB} = dsin\theta + dsin\theta\,. \tag{2.8}$$

If $\overline{OA} + \overline{OB}$ is equal to the integer number of X-ray wavelength (λ), it is considered as a constructive interference of scattered x-rays. Hence:

$$\overline{OA} + \overline{OB} = dsin\theta + dsin\theta = n\lambda, \tag{2.9}$$

$$2dsin\theta = n\lambda \tag{2.10}$$

where n = 1, 2, 3, d is d-spacing, the repeating distances planes of atoms in the structure. The Equation 2.10 explains the angular position of the diffracted beam and is also known as Bragg's Law. It is important to note that θ used in Bragg's Law is the angle between the diffraction plane and the incident radiation. However, in experimental setups X-ray

diffraction is usually expressed in terms of 2θ, which is the angle between the transmitted and Bragg diffracted beams because of the geometry of the Bragg's condition. In complex crystal structures, it is likely to consider planes of unit cell instead of planes of atoms. The phase and intensity of the waves scattered by each unit cell can be explained by structural factor.

The structural factor is the sum scattered waves from all the atoms in the unit cell, and it depends both on the position of each atom and its scattering factor. The structural factor can be expressed as:

$$F(hkl) = \sum_j f_j \exp[2\pi i(hu_j + kv_j + lw_j)], \qquad (2.11)$$

where f_j is the scattering factor of atom j and u_j, v_j, and w_j are the fractional coordinates in the unit cell. The structural factor also depends on the distribution of atoms in the unit cell, which affects the phase and the amplitude of the scattered wave.

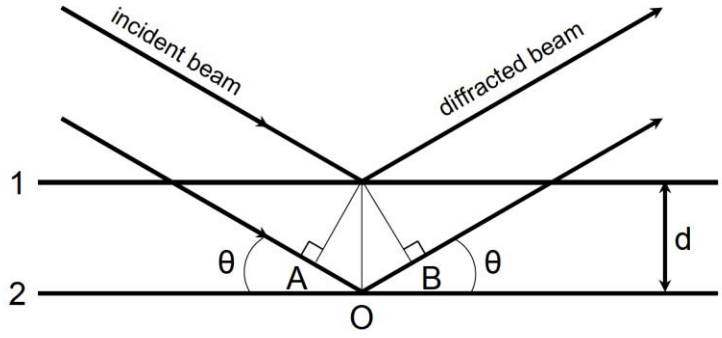

Figure 2.5 The geometry of X-ray reflection by planes of atoms in a crystal [85, 86].

X-ray diffraction pattern is a unique for each crystalline structure. The main x-ray diffraction parameters are peak position, shape, full width at half maximum (FWHM), maximum intensity and symmetry of the peaks. Those parameters are useful for the

crystalline structure analysis. The position of the diffraction peaks, the intensity of the peaks, and the number of the peaks identify the exclusive crystalline structure for every solid material. The number of peaks in the pattern are related to the symmetry of the unit cell. The unit cells with high symmetry usually result in less number of diffraction peaks in the pattern.

Every peak in the X-ray diffraction pattern represents a unique set of planes in the crystalline structure that are oriented on different directions. The different sets of planes and their orientation with respect to the unit cell are denoted by Miller indexes (h, k, l):

$$\left(\frac{a}{h},\ 0,\ 0\right) \text{ and } \left(0,\ \frac{b}{k},\ 0\right) \text{ and } \left(0,\ 0,\ \frac{c}{l}\right) \tag{2.12}$$

The peak position corresponds to the distance (d_{hkl}) between the reflection planes (hkl) with the fixed x-ray wavelength. To determine the peak position, the following techniques can be used. Those techniques are determining peak position directly from the diffraction angle at the maximum before and after smoothing or fitting the measured line with the mathematic function. The position of the peaks in the pattern can be also used to analyze the lattice parameters for a particular unit cell. Table 2.1 lists seven main crystal structures based on the length of three dimensions (a, b, and c) and three angles (α, β, and γ).

Table 2.1. The seven crystal systems and the restrictions placed on the lattice parameters of the unit cell [67].

Crystal System	Lattice Parameter Restrictions
Cubic	$a = b = c$ $\alpha = \beta = \gamma = 90^{\circ}$
Tetragonal	$a = b \neq c$ $\alpha = \beta = \gamma = 90^{\circ}$
Orthorhombic	$a \neq b \neq c$ $\alpha = \beta = \gamma = 90^{\circ}$
Monoclinic	$a \neq b \neq c$ $\alpha = \beta = 90^{\circ}; \gamma \neq 90^{\circ}$
Triclinic	$a \neq b \neq c$ $\alpha \neq \beta \neq \gamma \neq 90^{\circ}$
Hexagonal	$a = b \neq c$ $\alpha = \beta = 90^{\circ}; \gamma = 120^{\circ}$
Trigonal	$a = b \neq c$ $\alpha = \beta = 90^{\circ}; \gamma = 120^{\circ}$

X-ray diffraction is useful to calculate crystallite size of the material. It is important to understand the difference between grain size and crystallite size of the material. A crystallite is a single domain of solid-state structure that consists of a single phase. A grain consists of a single material and can be either crystalline or polycrystalline. The crystallite size of the coherent-diffraction-domain size can be found from Scherrer equation [87]:

$$L = \frac{K\lambda}{\beta cos\theta}, \tag{2.13}$$

where β is the peak width of the diffraction peak profile at half maximum height (in radians), λ is X-ray wavelength (in nanometers). The diffraction angle θ can be in degrees or radians, since the cosθ corresponds to the same number. K is a constant related to crystallite shape and index hkl. Crystalline size can be estimated by Scherrer formula with

K=1. However, for more precise calculation, K needs to be estimated as a function of crystal form and indices hkl.

The full width at half maximum (FWHM) is a width of the diffraction peak at a height half-way between background and the peak maximum. FWHM contains the information about average dimension of a crystalline size. The broadening of the peak is also one of the important factors to evaluate crystalline volume average size or area-average size. A decrease in the crystalline size causes an increase on the width of diffraction. The broader the peaks of the pattern indicates smaller crystallite size and less crystallinity of the material and its amorphous nature.

2.3.2 Scanning Electron Microscopy

The main part of a scanning electron microscope (SEM) is electrical column shown in Figure 2.6. The electrical column is held in high vacuum. It usually consists of the electron gun, magnetic lenses, scanning coils, backscattered electron detector, and secondary electron detector. When the high 10-20 kV voltage applied between the anode and the electron gun, the electron gun generates electron beam. This electron beam travels through electromagnetic fields and lenses to focus the beam towards the sample. The quality of image depends on the focus of the electron beam on the sample. The electric scanning coils allow the beam to move all over the sample [88]. Finally, a number of different signals such as X-rays, secondary electrons, and backscattered electrons are emitted from the specimen and collected in order to generate SEM image.

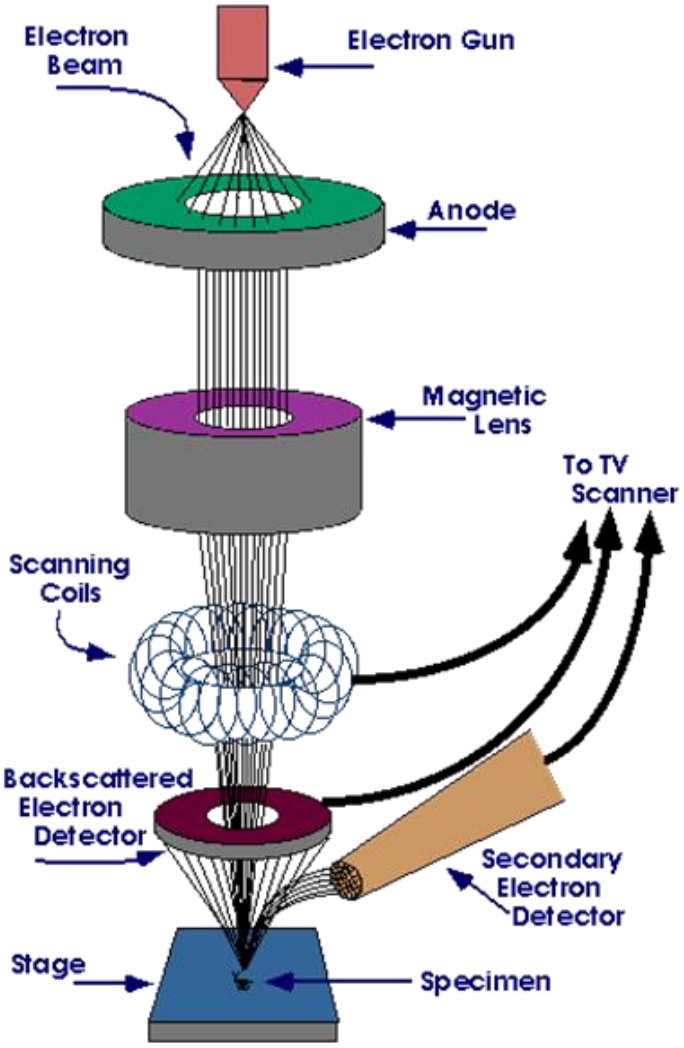

Figure 2.6 Main components of Scanning Electron Microscope [88].

Figure 2.7 represents a schematic of the incident beam on the sample. SEM detectors collect X-rays, secondary electrons, and backscattered electrons to transform them into a signal. This signal is sent to a computer to generate SEM image. Signals collected from the electron and sample interaction contain information about the morphology of the sample as well as chemical composition.

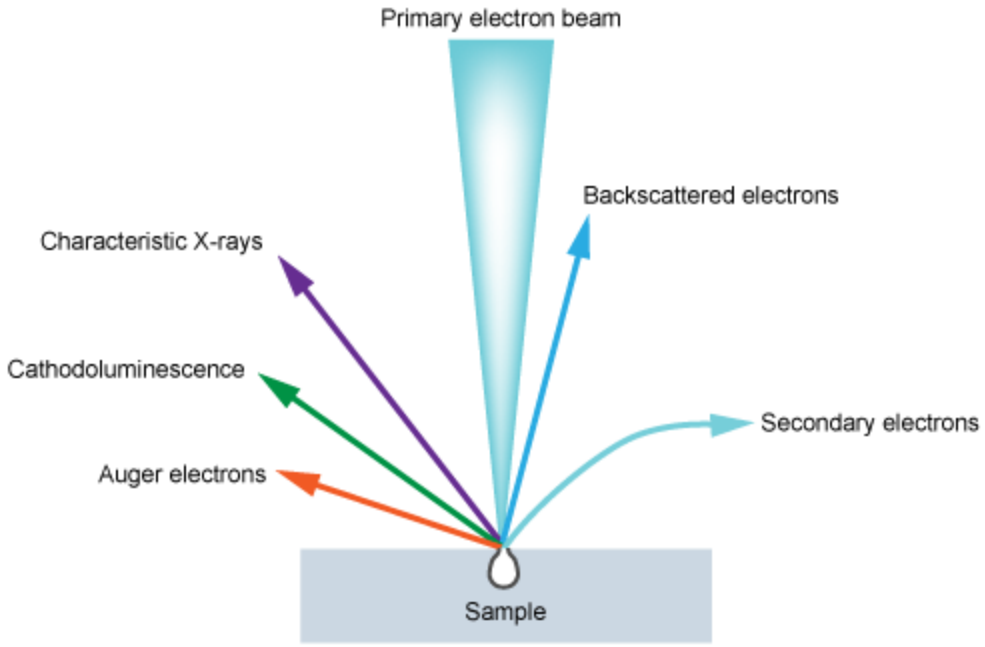

Figure 2.7 Effects of the incident beam on the sample [89].

Electrons generated by the gun and accelerated through electromagnet field and magnetic lenses carry kinetic energy that is dissipated into the sample. This energy is dissipated and collected in the form of secondary electrons, backscattered electrons, diffracted backscattered electrons, X-rays, visible light, and heat. The secondary electrons are used to generate SEM image. The backscattered and diffracted backscattered electrons are used to determine the crystal structures of the material. X-rays are used to determine the chemical composition and elemental analysis. X-ray are generated by inelastic collisions of the incident electrons with electrons in discrete orbitals of atoms in the sample. When the excited electron returns to its ground state, it generates X-rays of a fixed wavelength. This wavelength is related to the electron energy level difference of the specific element. X-rays generated by electron interactions do not cause the volume loss of the material, hence SEM analysis is considered as non-destructive characterization method.

2.3.2 Atomic Force Microscopy

Atomic Force Microscope (AFM) is one of the most advanced tools used for imaging the surface at the nanoscale level. The signals are collected by an ultra-sharp tip scanning over the surface of the sample. Figure 2.8 shows the schematic of the main AFM components. The main components of AFM tool are a piezo scanner, laser diode, a cantilever, and diode laser detector. The sample is placed on the sample holder stage located below the piezo scanner. The piezo scanner consists of three electrodes that precisely scan the surface of the sample in x- and y-direction and move the sample in z-direction. A cantilever is mounted to the lower end of piezo scanner via spring clip at one end. The other end of the cantilever equipped with a tip radius of curative on the order of nanometers. When the tip is placed close to a sample surface, the tip and the sample start to interact. The forces between the sample surface and the tip cause a deflection of the cantilever in agreement with Hooke's law [90]. When a laser beam from the laser diode is focused on to the surface of the cantilever, the laser beam is deflected due to the cantilever and sample interaction. The deflection of the laser is measured by the detector. AFM is capable to detect variety signals such as van der Waals forces, electrostatic forces, mechanical contact force, and magnetic forces. During the scanning process, the tip interacts with the topographic features of the sample surface, which causes the deflection of the cantilever. This causes the reflected laser beam to change the direction thus the intensity of AFM signal. To adjust the distance between the tip and the sample and maintain a constant force between the tip and the sample, the feedback mechanism is applied. The deflection signal creates the deflection image, and the feedback signal is used to create AFM height image.

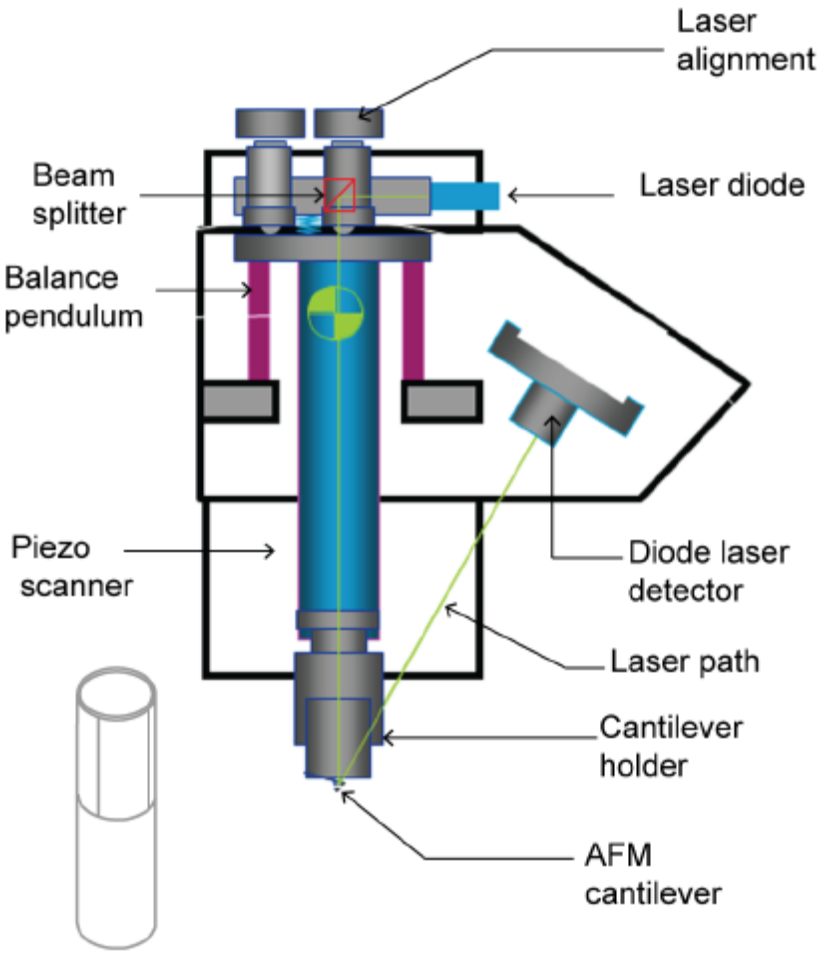

Figure 2.8 Block diagram of Atomic Force Microscope [91].

AFM can operate in three different modes depending on the tip and sample interaction forces as represented in Figure 2.9. When the tip is not in the contact with the sample and placed in the distance of attractive forces, the imaging is done in non-contact mode. If the tip is placed in mechanical contact with the sample surface in the net of repulsive forces, the imaging is carried out in the contact mode. In the case when the tip oscillates between attractive and repulsive forces, the imaging regime then called as tapping mode [92, 93].

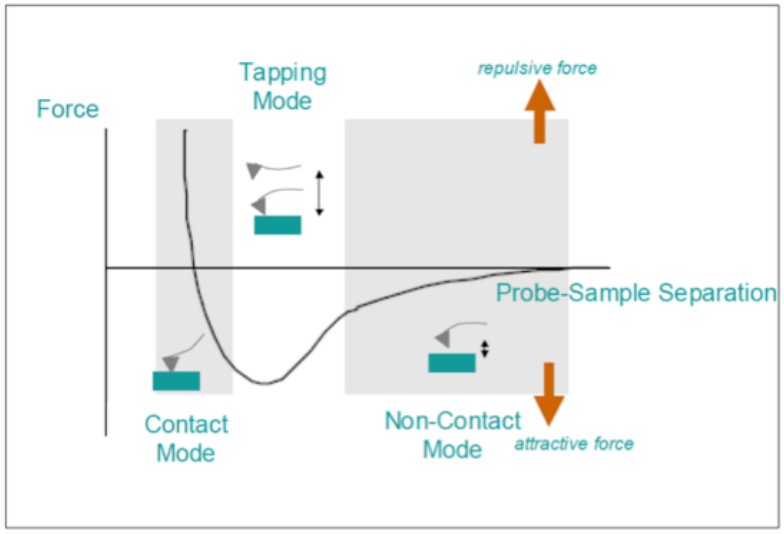

Figure 2.9 Force vs distance diagram and AFM imaging modes [94].

Tapping mode is typically used for high resolution topographic and phase images. This mode is also called as intermittent contact mode. A firm cantilever oscillates nearly the surface of the sample. The enhanced lateral resolution and elimination of drag over soft samples are advantages of tapping mode compared to standard contact mode. In contact mode, the tip is touching the surface of the sample and continuously in tune to maintain a constant deflection. The adjustment of the deflection is used to generate the image.

2.3.2.1 Current Sensing Atomic Force Microscopy

Current Sensing Atomic Force Microscopy (CS-AFM) is an advanced Scanning Probe Microscope (SPM) mode capable for studying of localized electric properties of a sample. It is very useful for electrical characterization of variety of materials including semiconductors, conducting polymers, ferroelectric films, dielectric films, etc. I also can be used for studying charge transport processes in single molecules. CS-AFM is suitable for localizing defects in thin films and for determining electronic and ionic processes in

cell membranes. It has proven useful in joint I/V spectroscopy and contact force experiments as well as contact potential studies.

CS-AFM operates in contact mode with the use of electrically conductive cantilever. An electrical current generates upon applying a voltage bias between the conductive cantilever and the sample substrate. The current signal is being collected and the conductivity image is created. During CS-AFM mode, the topography and conductivity images are generated simultaneously. This allows for direct correlation of local topography with electrical properties at nanoscale [95]. When the topography image is generated, the local current vs. voltage measurements are possible. During the characterization of the thin film samples, the conductive tip can behave as a metal electrode with the area determined by the tip-sample contact region.

2.3.2.2 Kelvin Probe Atomic Force Microscopy

Kelvin Probe Atomic Force Microscopy (KPAFM) or Surface potential microscopy is based on AFM setup and operates in non-contact mode. KPAFM determines the work function based on the electrostatic forces between the tip and the sample [96]. When the tip and the sample are brought in contact, a net electric current starts to flow between them until the Fermi levels were aligned. The conducting tip and the sample material can be characterized by work functions. The work function is the difference between the vacuum level and the Fermi level. The difference between the work functions of the tip and the sample is called the contact potential difference (CPD) [97].

A conductive tip oscillates at the first resonant frequency of the cantilever during the scan. The topographic data is taken by controlling the atomic force between the tip and

sample. Besides the atomic force, an electrostatic force exists between tip and sample because of the electric field between them. This electrostatic force determines the contact potential difference between the tip and the sample. In this system, the cantilever is a reference electrode that forms a capacitor with the surface of the sample [98]. For the measurement a voltage (V) is applied between tip and sample, consisting of a DC bias V_{DC} and an AC voltage $V_{AC}\sin(\omega t)$ of frequency ω. The electrostatic force is detected by applying an alternating current AC voltage to the tip and using a lock-in amplifier. In order to avoid the interaction between the topographic and electric signals, the AC voltage frequency is usually set either at the second resonant frequency or far off the first resonant frequency [99]:

$$V = (V_{DC} + V_{CPD}) + V_{AC}\sin(\omega t), \tag{2.14}$$

where V_{CPD} is the contact potential difference.

The electrostatic force (F) can be found by differentiating the energy function with respect to the separation of the elements

$$F = \frac{1}{2}\frac{dC}{dz}V^2, \tag{2.15}$$

where C is the capacitance, z is the separation, and V is the voltage, each between the tip and the surface.

2.4 Charge transport at Metal - Semiconductor interface

It is important to understand the charge transport mechanisms at metal-semiconductor interface since they are present in every semiconductor device. Figure 2.10 shows the energy band diagram of metal-semiconductor junction. Depending on the

characteristics of the interface, metal-semiconductor junctions can behave either as a Schottky barrier or as an ohmic contact.

An ohmic contact is a metal-semiconductor junction that allows current to flow equally in both ways [100]. In case of n-type semiconductor, the work function of the metal should be smaller than the electron affinity of the semiconductor of close to it. In case of, p-type semiconductor, the work function of the metal should be larger than the sum of the electron affinity and the bandgap energy. It might be challenging to find a metal to create an ohmic contact to p-type semiconductors with a wide bandgaps similar to SiC anf GaN because the work function of most metals is less than 5 lots and a typical electron affinity is about 4 V [101].

Schottky barrier occurs when the difference between work functions of semiconductor and metal determines the potential barrier height. When metal makes a contact with semiconductor, a potential barrier is created at the interface from the separation of charges. Charge carriers must have sufficient energy to pass over the potential barrier [102].

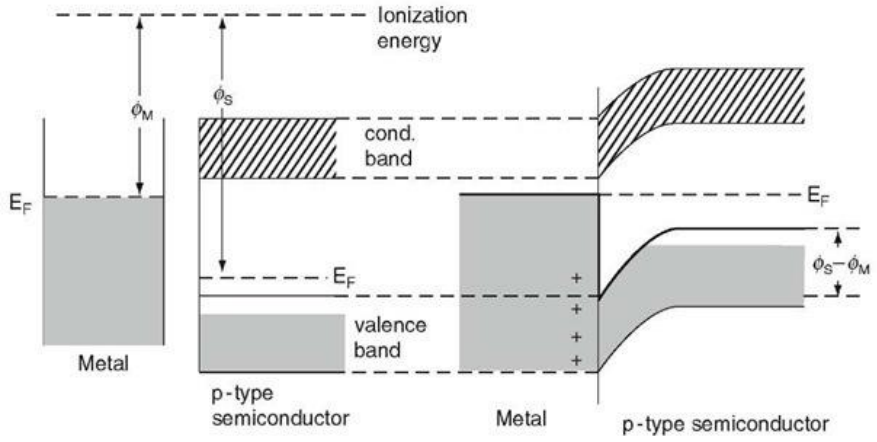

Figure 2.10 Energy band diagram of metal-semiconductor interface [85].

The Schottky barrier height can be expressed as:

$$\phi_b = \phi_m - \phi_s + E_c - E_f, \tag{2.16}$$

where φ_m is the work function of the metal, and the φ_s is the work function of the semiconductor, respectively. E_f is the fermi energy, and E_c is the conduction band of the semiconductor.

The Schottky diode equation can be expresses as:

$$I(V) = C(\exp(-DV) - 1), \tag{2.17}$$

where,

$$C = ART^2 \exp(-\frac{\phi_b}{k_B T}), \tag{2.18}$$

and

$$D = \frac{e}{k_B T}. \tag{2.19}$$

In the Equation (2.19) T is the temperature, K_b is Boltzman constant, e is electron charge, and R is coefficient:

$$R = \frac{4\pi m^* e k_B^2}{h^3}, \tag{2.20}$$

where h is Plank's constant and m* is electron effective mass.

Schottky emission model also can be applied to explain the current between semiconducting substrate and AFM tip (*I*):

$$I = Cexp(\frac{eV}{k_B T}). \tag{2.21}$$

where T is the temperature, V is the voltage applied between the tip and the sample, and C is the coefficient. The I-V curves measured by CS-AFM can be fitted using the Equation (2.19) to find C.

To find Schottky height barrier one can use the following equation:

$$\phi_b = k_B T ln(A_{eff} R T^2 / C \,, \tag{2.22}$$

where A_{eff} is the effective contact area between the semiconducting substrate and AFM tip.

If a semiconductor is doped strongly enough (10^{19} cm^{-3} or higher), it will form a potential barrier short enough for electrons to have a high probability of tunneling through. At the metal-semiconductor interface, if the width of the potential barrier is thin enough, within a range of few nanometers or even less, carriers can easily tunnel through this barrier. This type of contact is called a tunnel contact. The tunneling current depends on the barrier height. Tunneling is the quantum mechanics phenomenon when a particle can pass through the potential barrier due to a particles wave nature. The tunneling phenomenon is also studies at the metal-semiconductor interface.

The charge transport processes at metal-semiconductor interface and any DC current of a device can be divided into the ohmic regime, the space-charge-limited-current regime (SCLC), trap free voltage limit, and trap free SCLC regime as represented in Figure 2.11. In the ohmic regime, the current density is proportional to the electric field, $J \sim V$. This is equal to a sample resistance.

The space-charge-limited-current regime (SCLC) arises when the charge concentration is insignificant compared to the injected charge concentration. In SCLC, the current is proportional to the square of the electric field, $J \sim V^2$. This means that the charge concentration is high near the injecting electrode and decreases significantly away from the electrode. When higher bias applied, the trap levels are filled. This region is voltage trap free limit. Beyond this limit, the traps are occupied with free charges, and the device pass in the trap-free SCLC regime, $J \sim V^2$.

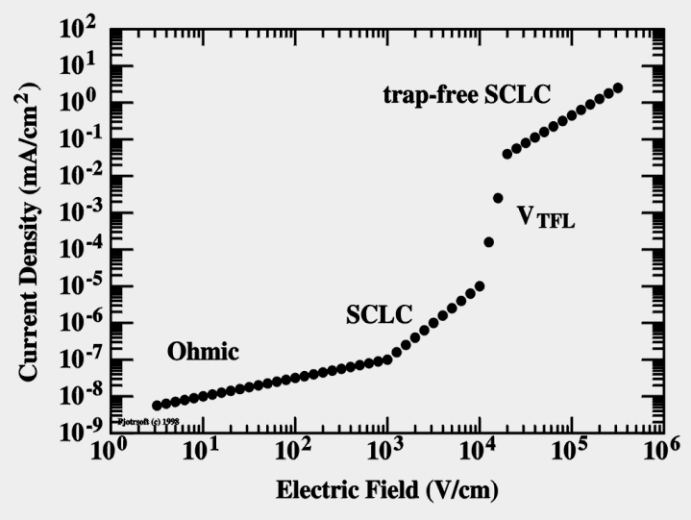

Figure 2.11 Types of DC current at metal-semiconductor interface [103].

The local J-V curves measured with CS-AFM can be used to extract local charge carrier motilities by fitting the data with the space charge limited current (SCLC) model [104]. The SCLC model is based on Mott-Gurney law and takes into account the ratio of the tip diameter to the sample thickness [105]. Fitting the CS-AFM J-V curves with SCLC model yields values of charge carrier mobility. In contrast, in ohmic conduction regime, the current is dominated by mobile charge carriers intrinsically presented in the material.

In SCLC system, the current dependent mostly on the mobility of charge carriers rather than the charge carrier density. It is driven by charge carriers injected from the contacts. These charge carriers cause a field gradient, which limits the current density. An electric field causes charge carriers to reach a specific drift velocity that is parallel to the direction of the field. This condition usually applies for doped semiconductors and insulating materials. The mobility (μ) is proportional to the magnitudes of the electric field (E) and drift velocity (v):

$$v = \mu E \tag{2.23}$$

The drift current Gauss's law can be expressed by

$$J = qp\mu E, \tag{2.24}$$

$$\frac{dE}{dx} = \frac{qp}{\varepsilon}, \tag{2.25}$$

where J is the current density, p is the carrier density, q is the elementary charge. The carrier density can be eliminated to yield:

$$\frac{J}{\varepsilon\mu} = E\frac{qE}{dx}, \tag{2.26}$$

After the integration from 0 to x, with the assumption that the electric field equals zero at x= 0:

$$\frac{Jx}{\varepsilon\mu} = \frac{E^2}{2}, \tag{2.27}$$

Integrating once again from x= 0 to $x = d$ with $V(0) = V$ and $V(d) = 0$, one finds:

$$V = \int_0^d E dx = \sqrt{\frac{2J}{\varepsilon\mu}}\frac{d^{\frac{3}{2}}}{3/2} \tag{2.28}$$

from which one obtains the expression for the space-charge-limited current based on Mott-Gurney law [106]: $J = \frac{9}{8}\varepsilon\mu\frac{V^2}{L^3}$, (2.29)

where J is the current density, V is applied voltage bias, L is the thickness of the thin film, μ is the charge carrier mobility, $\mathcal{E}$ is the relative dielectric constant of the thin film.

CHAPTER 3. EXPERIMENTAL PROCEDURES

This chapter discusses experimental procedures related to fabrication processing of lead free perovskite thin films and solar cell devices. The characterization techniques and procedures are also described.

3.1 Fabrication of $CH_3NH_3SnI_3$ perovskite solar cells

3.1.1 Preparation of photoelectrodes

Fluorine-doped tin dioxide glass substrates were dipped into acetone solution and ultrasonicated for 10 minutes. The substrates were then rinsed with de-ionized (DI) water, followed by ultrasonication for 10 minutes in isopropanol (IPA) solution. Finally, the substrates were rinsed with DI water and dried with compressed nitrogen gas.

3.1.1.1 4 nm TiO_2 particle synthesis

A magnetic stir bar and 240 mL of 0.1M HNO_3 were added to the 500-mL Erlenmeyer flask. The flask was placed on a stirring hotplate. 40 mL of titanium isopropoxide was slowly poured into the Erlenmeyer flask, with rapid stirring. The titanium isopropoxide instantly hydrolyzes when in contact with the nitric acid, forming titanium dioxide. Once all of the titanium isopropoxide has been added, the hotplate was set to 80°C, ensuring that the solution is still stirring rapidly. The reaction was run for 16 hours.

When the solution became a translucent white, the heat and stirring were turned off, and the solution was cooled for 10-15 minutes. A stir bar extractor was used to remove the magnetic stir bar, making sure not to touch the solution. Then, the Erlenmeyer flask was moved to the rotavap, and the hot water bath was set to 40°C. Once a solid that was obtained

became dry, the flask was removed from the rotavap, and the content was poured into the mortar. The solid TiO_2 was grind into a fine, consistent powder, using a mortar and pestle.

3.1.1.2 Compact TiO_2 sol-gel preparation

The 0.5 g of 4 nm TiO_2 particles was placed into a vial, and 2 g of DI was added. The vial with TiO_2 was sonicated until the TiO_2 dissolved into the water. Then, 0.2 g of Triton X-100 was added into the vial, and the solvent was sonicated again for 5-10 minutes to ensure that the Triton X-100 is evenly distributed throughout the solution.

3.1.1.3 Deposition of TiO_2 compact layer

The precursor 0.15 M and 0.3 M solution for compact TiO_2 was prepared using titanium diisopropoxide bis(acetylacetonate), 75 wt.% solution diluted in 2-propanol. Each layer made of 0.15 M and 0.3 M compact TiO_2 solutions were spin coated onto cleaned and dried FTO-glass substrates at 4500 rpm for 30 sec followed by annealing at 450 ˚C for 30 min and then cooled down to room temperature.

3.1.1.4 Deposition of active TiO_2 layer

1 g of TiO_2 (Dyesol 18NRT with particle size 20 nm) was diluted with 4.436 ml of ethanol and then the mixed solution was spin coated at 5500 rpm on top of the compact layer of TiO_2. The thickness of mesoporous TiO_2 is approximately 600 nm. The mesoporous TiO_2 coated substrates were annealed again at 450 ˚C for 30 min, and then cooled down to room temperature.

3.1.1.5 Post-treatment s of TiO_2 electrodes

The preparation of post treatment solution consists of 20 ml DI water and 55µl of $TiCl_4$. First, 55µl of $TiCl_4$ was added to 20 ml of DI water. The solution was placed inside refrigerator. The prepared TiO_2 substrates were placed inside vials and then treated with prepared $TiCl_4$ solution for 30 min at 70 ˚C. Then, the treated substrates were rinsed with DI water and then ethanol followed by annealing at 450 ˚C for 30 min. The substrates were cooled down to room temperature. Finally, substrates were transferred inside glove box for depositing the $CH_3NH_3SnI_3$ layer.

3.1.2 Preparation of the $CH_2NH_3SnI_3$ active layer

To prepare precursor solutions, equimolar quantities of CH_3NH_3I and SnI_2 with a concentration of 40 wt% was dissolved in a mixed solvent of DMF and DMSO-GBL with a ratio 3.5:7. The schematic of the active layer deposition is shown in Figure 3.1. The precursor solutions were spin coated onto TiO_2 coated substrates to form a dark-brown tin perovskite layer. Because the $CH_3NH_3SnI_3$ gradually decomposed in air, all the preparation of $CH_3NH_3SnI_3$ films were performed in nitrogen glove box to avoid hydrolysis and oxidation of tin perovskite layer in contact with ambient air.

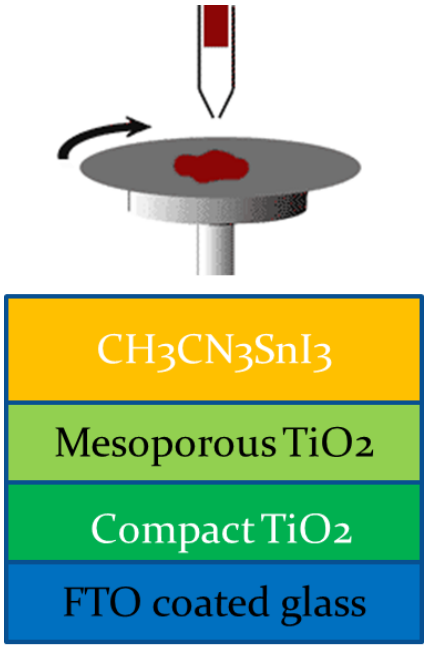

Figure 3.1 The schematics of the active layer of $CH_3NH_3SnI_3$ layer deposition.

3.1.3 Fabrication of counter electrodes

The counter electrode of 100 nm silver was prepared using thermal evaporation to form back contact of the device. The device fabrication and characterization was carried out under controlled environment inside a nitrogen glovebox.

3.2 Characterization of prepared devices and thin films

The characterization of fabricated counter electrodes was carried out with UV-VIS analysis, morphology analysis based on Scanning Electron Microscope, Atomic Force Microscope, and X-ray diffraction. The characterization of lead free perovskite device was based on current-voltage (I-V) measurements.

3.2.1 Current-Voltage (I-V) measurement

The schematic of experimental arrangements for current-voltage measurements for solar cell device is shown in Figure 3.2. The voltage power supply (Newport 6991C) was connected to the AM 1.5 filtered solar simulator (xenon (Xe) lamp, Newport 67005) and set to 300 watts. Xe lamp was turned on 20 minutes before the calibration of the light intensity from the solar simulator.

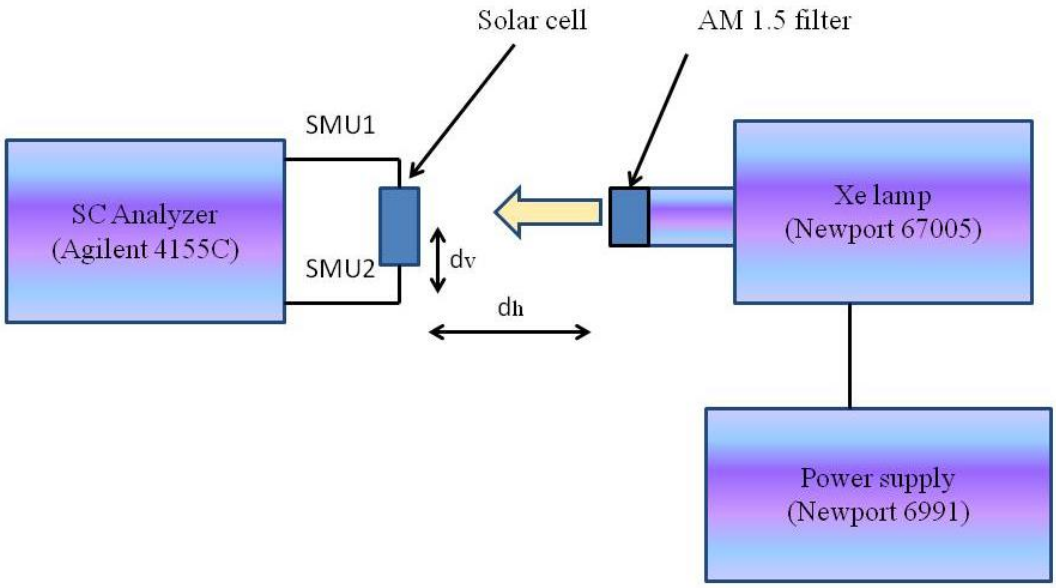

Figure 3.2 The schematic of experimental setup for IV measurements.

A reference cell, NREL calibrated Hamamatsu S1133-14 photodetector, was placed vertically in a sample holder as shown on Figure 3.3, so that the light from the solar simulator was normally incident on the solar cell.

The leads of the cell were connected to semiconductor (SC) parameter analyzer (Agilent 4155C), which measures the I-V response of the sample. SMU1 (source/monitor unit) sweeps the applied bias and SMU2 measures the current. The intensity of the lamp

was adjusted by verifying the vertical (d_v) and horizontal (d_h) distance between the reference cell and Xe lamp until the short circuit current (I_{sc}) was 1.63 mA. Appendix 1 provides the NREL document data for calibrated Hamamatsu S1133-14 photodetector. Once the light intensity of the lamp was calibrated, the reference cell was removed, and solar cells under test were placed in exactly the same place previously occupied by the reference cell so that the intensity of the light source was equal 1000W/m^2.

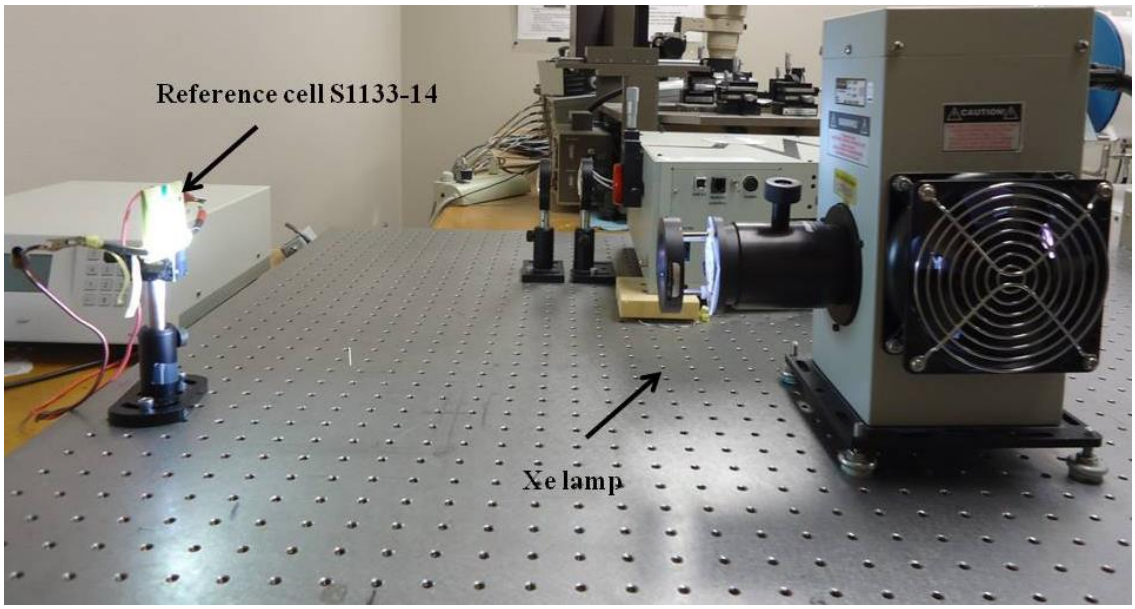

Figure 3.3 The experimental setup for calibrating the light intensity of solar simulator.

The biased voltage applied by Agilent 4155C SC Analyzer was swept from 0 V to +1 V in the step of 10 mV. The data of the bias voltage and corresponding current produced by the cell were measured and recorded under illuminated conditions.

3.2.2. Scanning Electron Microscopy

The morphology analysis was carried out using Hitachi Model S-3400N Scanning Electron Microscope. The $CH_3NH_3SnI_3$ samples were placed on the sample holder inside the nitrogen glovebox using conductive tape. Then, the samples were loaded in the SEM vacuum chamber immediately after they were taken outside of glovebox to avoid the degradation of the samples upon contact with oxygen and water molecules present in ambient air. The best quality images were taken under 15 kV applied bias.

3.2.3 UV-VIS spectroscopy measurements

Agilent 8453 UV-VIS spectrophotometer G1103A was used to measure absorbance spectra of $CH_3NH_3SnI_3$ films. Before measuring the absorption of samples the baseline correction was performed using blank sample. For accurate measurements, the blank and the sample absorption measurements closely followed each other. The blank sample was consisted of compact and mesoporous TiO_2 layers deposited on cleaned FTO-glass substrate. The fabrication procedure was described in section. The sample was placed in a sample holder, and the measurements were run by sweeping the wavelength from 300 nm to 1400 nm and recording the absorption at the specific wavelength.

3.2.4 X-ray Diffraction

X-ray diffraction data was measured by Rigaku SmartLab diffractometer. The wavelength of the X-ray source was 1.54 A generated by copper tube when 44keV of accelerated voltage was applied. The x-ray was scanned from 10º to 80º of 2θ axes. The samples we placed on the sample holder horizontally and kept stationary. Figure shows a picture of XRD experimental setup. The x-ray source, the detector, and sample can be

rotated by goniometer. The source of X-ray and the detector are rotating along z- as shown in Figure 3.4, and the X-ray beam intensity is recorded as a function of 2θ.

Figure 3.4 Photo of X-ray Rigaku SmartLab diffractometer.

3.2.5 Atomic Force Microscopy

AFM measurements were conducted using an Agilent 5500 microscope inside a glove box under dry nitrogen environment. AFM imaging was performed using Picoview 1.14.2 software provided by Keysight technology. This dedicate software tool employs a specific algorithm to determine the peaks and valleys for the surface morphology. The segmentation method can be applied to determine grain or particle sizes. The images were processes using Gwydion software. The measurements were performed on FTO/TiO_2/$CH_3NH_3SnI_2$ substrates. Different areas of the samples were scanned to confirm the consistency of the results. All AFM measurements were performed in a hermetically sealed glovebox chamber under dry nitrogen atmosphere.

3.2.5.1 Current Sensing Atomic Force Microscopy

Current Sensing Atomic Force Microscopy was used to perform local current mapping and topography over the sample surface. The experimental setup is presented on Figure 3.5. The ultra-sharp conducting probe makes a contact with a sample surface and measures the current signal as a function of applied bias. The conductive tip acts as metal contact probe with an active area determined by tip-sample contact region. The applied bias is either applied voltage or optical bias. A voltage bias can be applied between the tip and the sample while cantilever is kept at virtual ground. An optical bias can be applied by illuminating a small area on the sample from the bottom with 0.5 sun illumination. The current signal generated as a function of applied bias is used to construct the image.

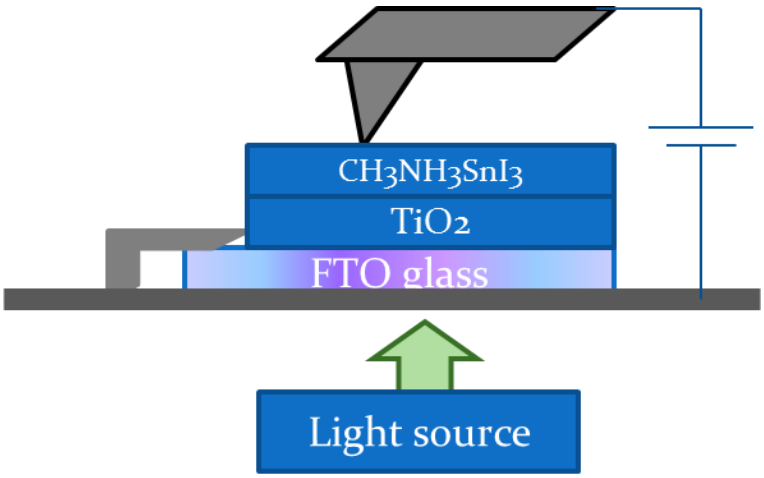

Figure 3.5 The experimental setup of characterization of $CH_3NH_3SnI_3$ film using AFM.

Agilent 5500 AFM was equipped with a special 4-pin nose cone containing a build-in preamplifier shown in Figure 3.6. The sensitivity of the preamplifier was 0.1 nA/V and operational range from 1 pA and 1 nA. The measurements were performed in contact mode

using Al coated Si tip (Budget Sensors, radius 20 nm, tip force was 0.2 N/m, resonance frequency ≈14 kHz). The deflection of the cantilever was held constant throughout the scan to maintain a constant force between the tip and the sample. The measurements were performed at the lowest set point regimes when the tip softly touches the surface, which is important to collect the signal without damaging the surface of the sample. The scan speed was 0.45 l/s.

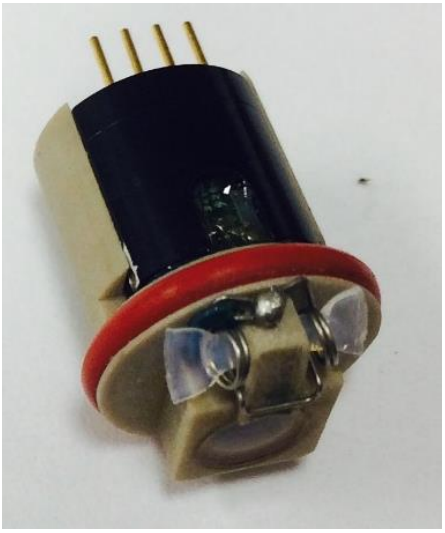

Figure 3.6 4-pin current sensing nose cone equipped with a build-in preamplifier.

Current sensing images and topography images were taken simultaneously. In this experimental setup, the background noise was about 5 pA and any current signal above this level was detectable. The local current was measured as a function of the applied electrical bias at certain points on the surface producing local I-V plots. While measuring local I-V, the feedback loop was enabled to ensure that the force applied by the cantilever was kept constant. After every I-V measurement, the same region was scanned again to ensure that there no damage to the sample surface occur.

The sample stage was modified in the way that it had an ample room at the bottom where the sample was illuminated with the laser as can be seen from the Figure 3.7. To avoid leakage of current/voltage during CS-AFM measurements, the stage was modified in the way that there is no electrical contact between the sample and the stage flat platform that is grounded.

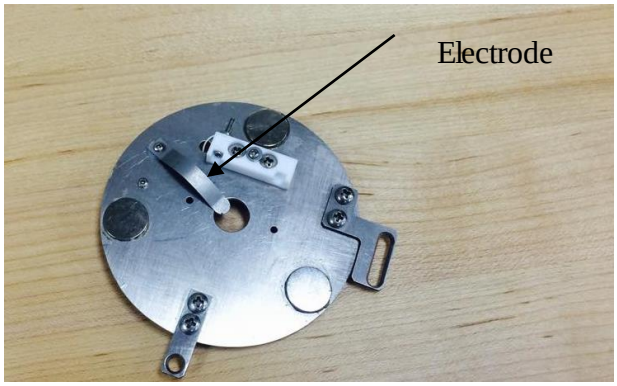

Figure 3.7 Sample stage for CS-AFM measurements.

The contact between the electrode bolt and the stage platform was isolated with plastic washer. After that all the contacts were checked with voltmeter to assure that all contacts are secure. The modifications were made at SDSU Electrical Engineering department machine shop.

3.2.5.2 Kelvin Probe Atomic Force Microscopy

Surface potential measurements were performed using Agilent SPM 5500 Atomic Force Microscope equipped with a MAC III controller, which consist of three lock-in amplifiers. A Budget Sensors Multi 75-EG tip with Pt-Ir coating was used for scanning. The first resonant frequency of 67 kHz was fed into the first lock-in amplifier, and the

second resonant frequency of 5 kHz was fed into the second lock-in amplifier. The first lock-in amplifier was used to conduct the topography and phase imaging while the second lock-in amplifier was used for surface potential (KPAFM) measurements. The electrostatic amplitude of 0.2 V was achieved with the DC offset of -3V and the 15% drive percentage of the second lock-in amplifier All KPAFM measurements were carried out inside the glove box with O_2 and H_2O level < 0.1 ppm to eliminate the effect of oxidation of the samples.

CHAPTER 4. RESULTS AND DISCUSSION

Chapter 4 presents the results from the experiments outlined in chapter 3. This chapter includes results and discussion from X-ray diffraction, UV-VIS, surface morphology, and optoelectrical characteristics of $CH_3NH_3SnI_3$ perovskites in comparison with $CH_3NH_3PbI_3$.

4.1 $CH_3NH_3SnI_3$ perovskites compared to $CH_3NH_3PbI_3$ counterparts

To point the differences and similarities of $CH_3NH_3SnI_3$ and $CH_3NH_3PbI_3$ material structure, XRD measurements were performed. Figure 4.1 shows XRD data of (a) $CH_3NH_3SnI_3$, (b) $CH_3NH_3PbI_3$, and (c) TiO_2 recorded from Rigaku SmartLab diffractometer. Peaks at 26°, 34°, 38°, 45°, and 52° shown in Figure 4.1 (c) attributed to TiO_2 and FTO and having anything to do with the perovskite itself [107]. As can be seen from Figure (a) and (b) 14°peaks were pretty similar for both tin and lead based perovskites. However, the intensities of the peak were different. The intensity of tin based perovskite film was showing higher intensity at 14°, which will be discussed later in this section. Peaks at 25°, 28°, 32°, 41°, and 43° can be attributed to $CH_3NH_3SnI_3$ were observed as similar to the literature [43].

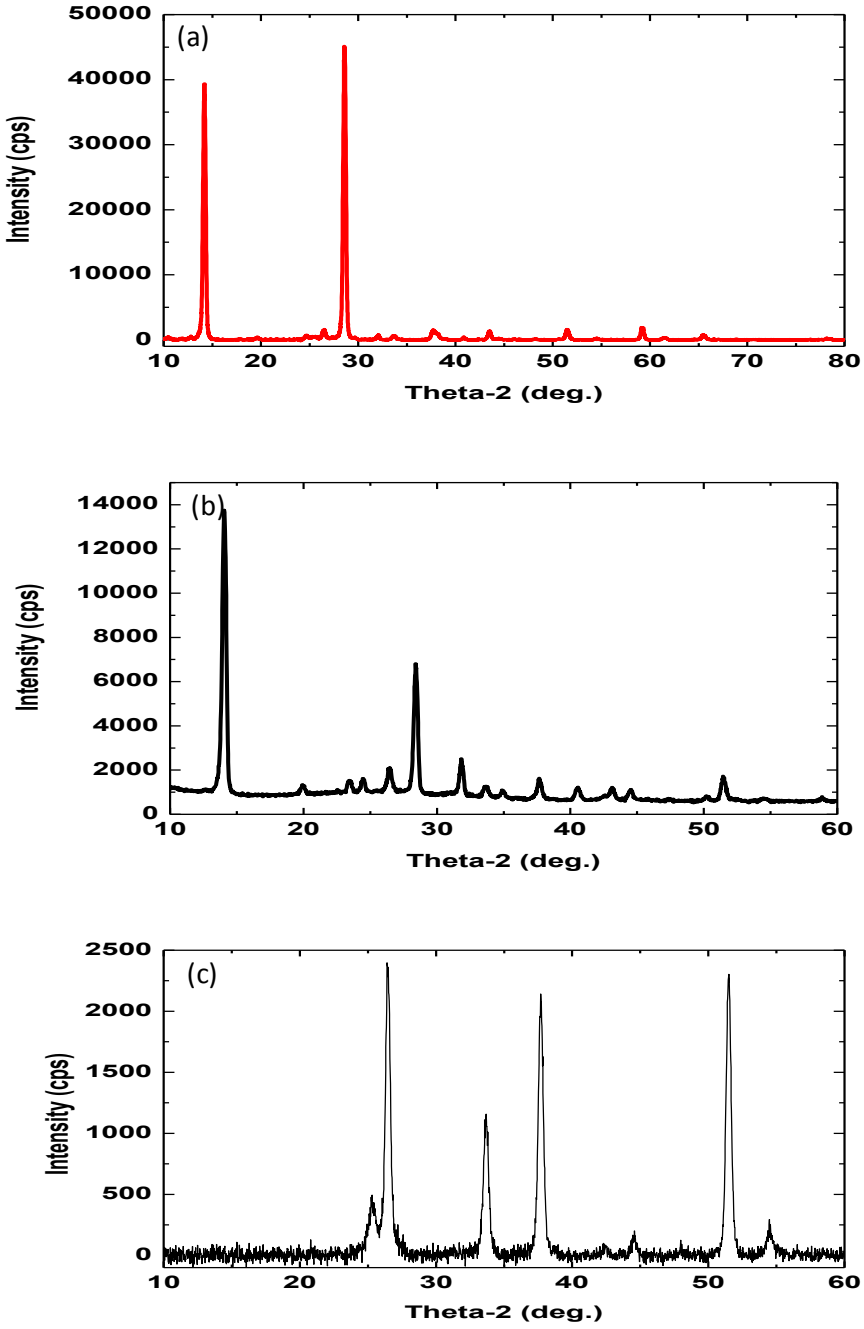

Figure 4.1 XRD spectra of (a) $CH_3NH_3SnI_3$, (b) $CH_3NH_3PbI_3$, and (c) TiO_2 films.

Optical absorption of $CH_3NH_3SnI_3$ film compared to $CH_3NH_3PbI_3$ film are shown in Figure 4.2. As can be seen from the figure lead based thin film has higher absorption from 350 nm to 570 nm with sharp absorption edge of 770 nm. The optical (UV-VIS) absorption of $CH_3NH_3SnI_3$ thin film on the other hand shows broader absorption spectrum with absorption edge at approximately 1000 nm, which was in agreement with other literature [52].

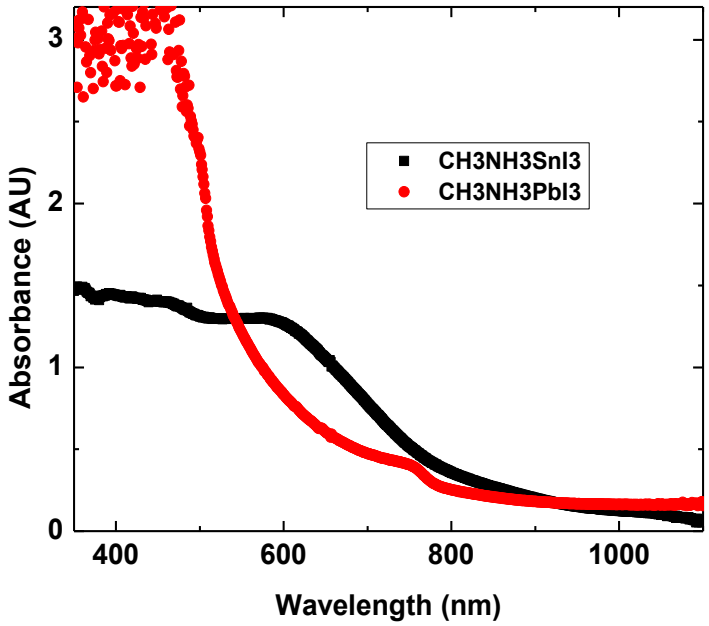

Figure 4.2 UV-VIS absorption spectra of $CH_3NH_3SnI_3$ film compared to $CH_3NH_3PbI_3$ film.

SEM images of $CH_3NH_3SnI_3$ film compared to $CH_3NH_3PbI_3$ film are represented in Figure 4.3. The lead based films showed uniform film with great degree of coverage whereas tin based films showed big (10-15 μm) crystalline platelets in addition to the material that penetrates to the pores of mesoporous TiO_2 [52]. Those platelets were unevenly distributed all over the surface of the film. Some of them are closely packed

together while others were distant from each other. These crystalline platelets can explain the high intensity peaks of tin based film observed in XRD data. Since $CH_3NH_3SnI_3$ film crystallizes at room temperature, these crystalline formations of top of the surface were formed during the spin-coating process. Lead based thin film requires heating and crystalized during the annealing process.

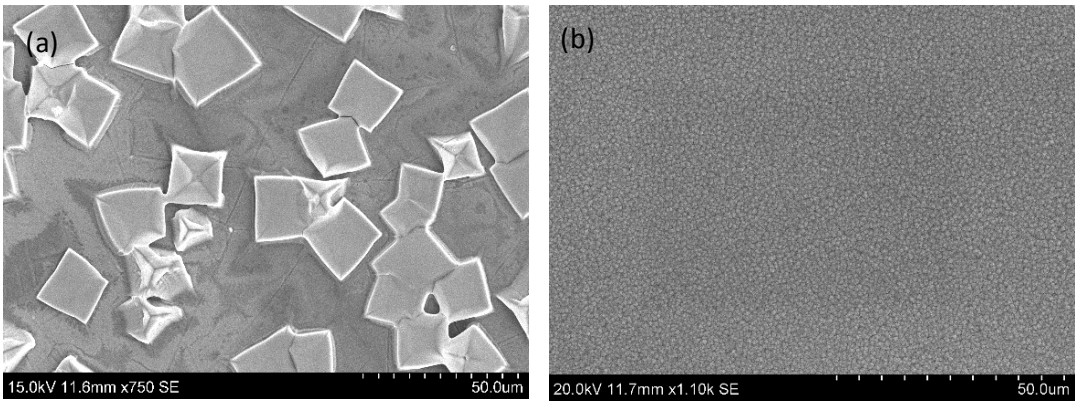

Figure 4.3 SEM images of (a) $CH_3NH_3SnI_3$ film compared to (b) $CH_3NH_3PbI_3$ film.

AFM topography image 5x5 um of (a) $CH_3NH_3SnI_3$ film and (b) $CH_3NH_3PbI_3$ film are shown in Figure 4.4. The grains varying in size between 20 and 200 nm were found in both structures. The tin based film had a surface roughness (Rrms) of 13.18 nm and lead based film surface roughness of 10.75 nm.

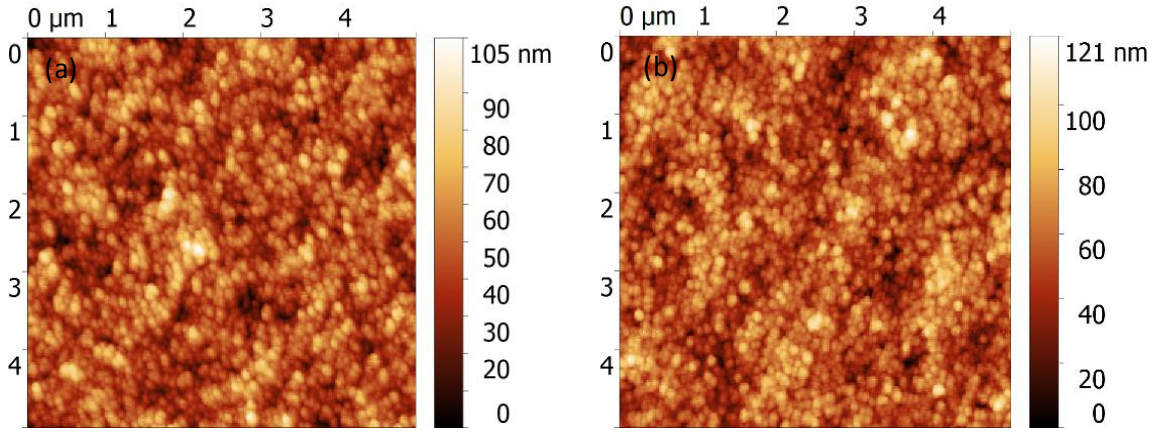

Figure 4.4 AFM topography images of (a) $CH_3NH_3SnI_3$ film compared to $CH_3NH_3PbI_3$ film.

Local current signal from CS-AFM mapping of (a) $CH_3NH_3SnI_3$ film and (b) $CH_3NH_3PbI_3$ film are presented in Figure 4.5. Cr-Pt tip was used to collect the local CS-AFM current signal. In the dark and without applying electrical bias, there was no noticeable current observed for both samples. The measured current was in the range of between 300 fempto Amps to 431 fempto Amps, which can be attributed to the background noise of the instrument. This indicates a negligible effect of topography on current images.

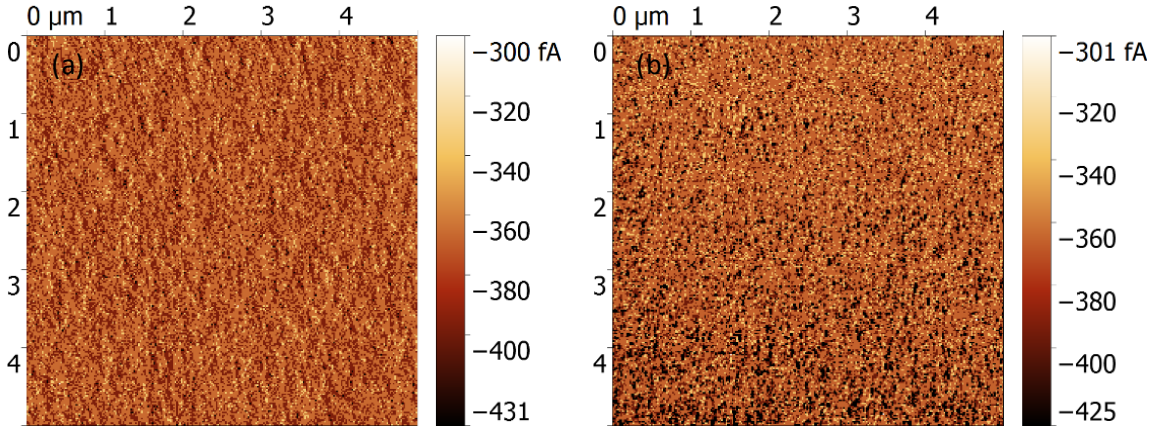

Figure 4.5 CS-AFM images performed in the dark at 0 V for the sample processed from (a) $CH_3NH_3SnI_3$ film compared to (b) $CH_3NH_3PbI_3$ film.

Photocurrent mapping of (a) $CH_3NH_3SnI_3$ film and (b) $CH_3NH_3PbI_3$ film are presented in in Figure 4.6. When illuminated, the maximum short-circuit photocurrent of $CH_3NH_3SnI_3$ was ≈ -916 fempto A, whereas maximum in photocurrent of $CH_3NH_3PbI_3$ was ≈ -29pA. This indicates that the lead based film extracts more excited charge carriers compared to tin based thin film. The reason for low local photocurrent of tin based thin film can be attributed to the work function mismatch between Cr-Pt tip and conduction band of $CH_3NH_3SnI_3$, which can a barrier for the collection of holes. This indicates that the conduction band of $CH_3NH_3SnI_3$ is higher compared to $CH_3NH_3PbI_3$.

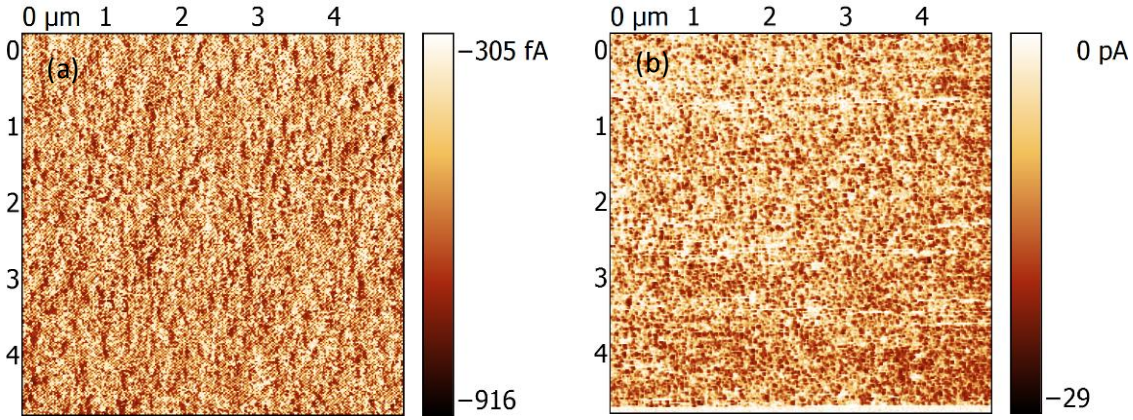

Figure 4.6 CS-AFM images when illuminated at 0.5 sun illumination and 0 V bias voltage for the sample (a) $CH_3NH_3SnI_3$ film compared to (b) $CH_3NH_3PbI_3$ film.

A schematic of nanoscale charge injection and energy band diagram of (a) $CH_3NH_3SnI_3$ compared to (b) $CH_3NH_3PbI_3$ are shown in Figure 4.7. The values of energy band diagrams were choosen as from the litersture [42, 108, 109]. Under illumination, the electrons were promoted from the valence band to the conduction band of $CH_3NH_3SnI_3$ of $CH_3NH_3PbI_3$ film, transferred to TiO_2 and collected at the FTO electrode. The holes were collected by Cr-Pt tip, meaning that the current from CS-AFM measurements may be considered as a hole current. Since the direction of hole current under illumination was toward the tip, the measured values of the CS-AFM current have negative value as can be seen from Figure 4.7. It can be seen that Cr-Pt tip was not a good match for the holection of hole. This also means that to make a good working $CH_3NH_3SnI_3$ device the materials for the hole transport layer and back contact electrole should have a work function higher than the conduction band of $CH_3NH_3SnI_3$.

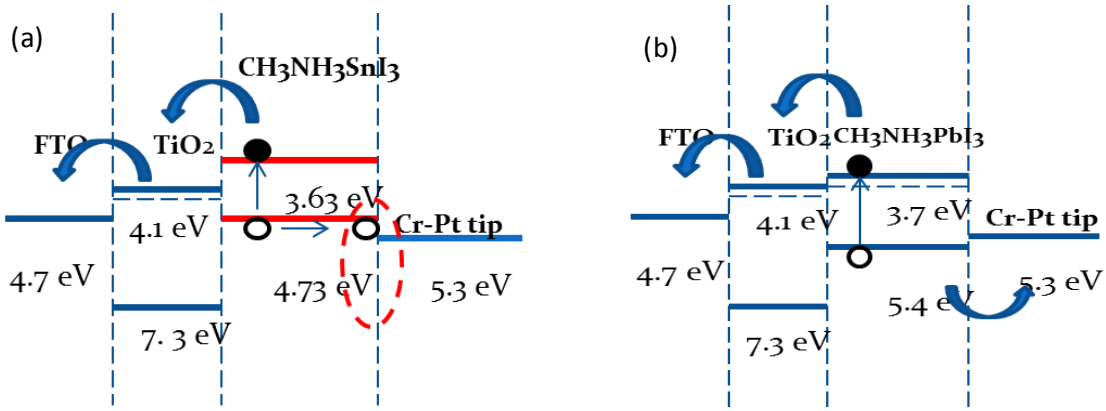

Figure 4.7 Band diagram showing charge collection of photocurrent of (a): $CH_3NH_3SnI_3/TiO_2$/ FTO/glass heterojunction compared to (b): $CH_3NH_3PbI_3/TiO_2$/FTO/glass heterojunction structure using Cr-Pt-coated conductive tip.

Figure 4.8 shows CS-AFM images under positive (+1V) bias applied on FTO electrode for (a) $CH_3NH_3SnI_3$ and (b) $CH_3NH_3PbI_3$ films. The local current of $CH_3NH_3SnI_3$ film under positive bias reached up to 1 nA whereas the local current of $CH_3NH_3PbI_3$ film was up to 0.7 nA. It confirmed that $CH_3NH_3SnI_3$ can be a good electron transporter. However, in case of $CH_3NH_3SnI_3$ there is a tendency towards oxidation which causes the material to be doped with Sn^{4+} thus behaving as p-type upon oxidation [46].

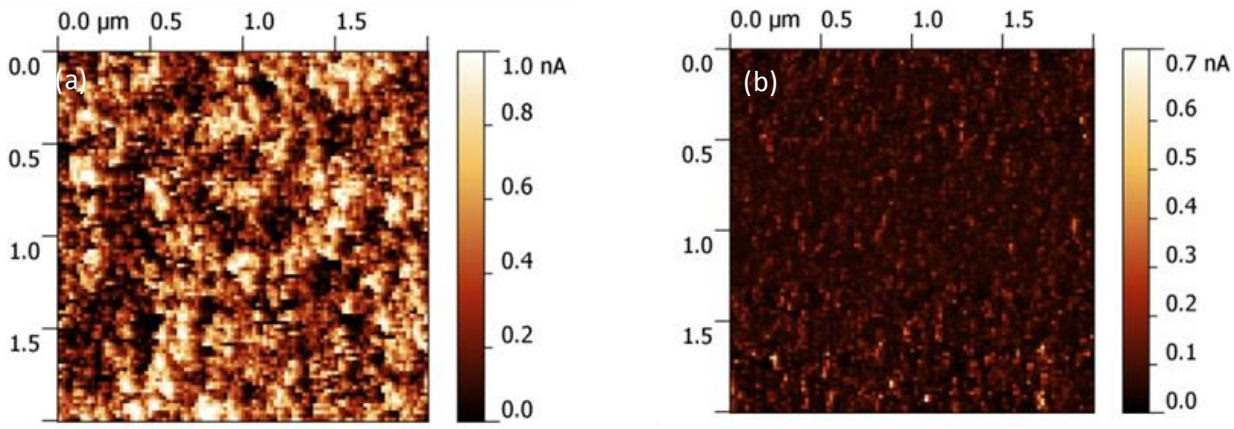

Figure 4.8 CS-AFM images when positive (+1V) bias applied on FTO electrode for (a) $CH_3NH_3SnI_3$ and (b) $CH_3NH_3PbI_3$ films.

Figure 4.9 shows AFM topography (a), (c) and surface potential (b), (d) 1µmx1 µm images of $CH_3NH_3SnI_3$ and $CH_3NH_3PbI_3$ films, respectively. The grain size of lead based film was around 200 nm while that of tin based film was around 400 nm. It can be seen that the sirface potential of lead based perovskites was higher than tin based film. The maximum surface potential difference of $CH_3NH_3SnI_3$ is 0.19 V while $CH_3NH_3PbI_3$ has its maximum of 0.3 V. The higher surface potential of $CH_3NH_3PbI_3$ film can be attributed to lower surface defects caused by dandling bonds. These dangling bonds act as a trap center for electrons [28]. It was also noticed that surface potendial difference is not even all over the surface for both samples.

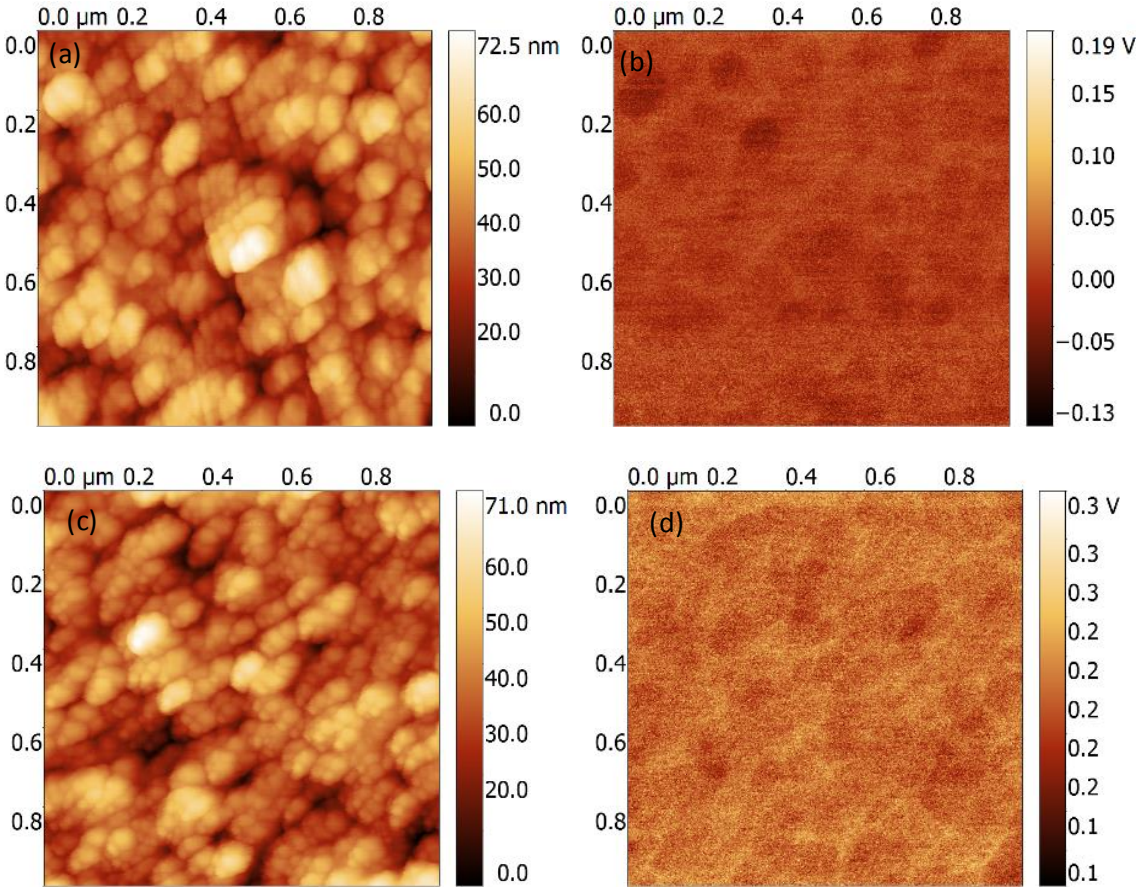

Figure 4.9 AFM topography (a), (c) and surface potential (b), (d) 1µm x1µm images of $CH_3NH_3SnI_3$ and $CH_3NH_3PbI_3$ films, respectively.

For more detailed analysis of surface potential difference and morphology of both films, the line scanning profiles of topography and surface potential are presented in Figure 4.10. From line profiles of both $CH_3NH_3SnI_3$ and $CH_3NH_3PbI_3$ can be seen that higher surface potential was at grain boundaries rather than within the interior of the grains. This was attributed to downward energy band banding at the edge of grain boundaries, which can be addressed to minority carriers in p-type material [110, 111].

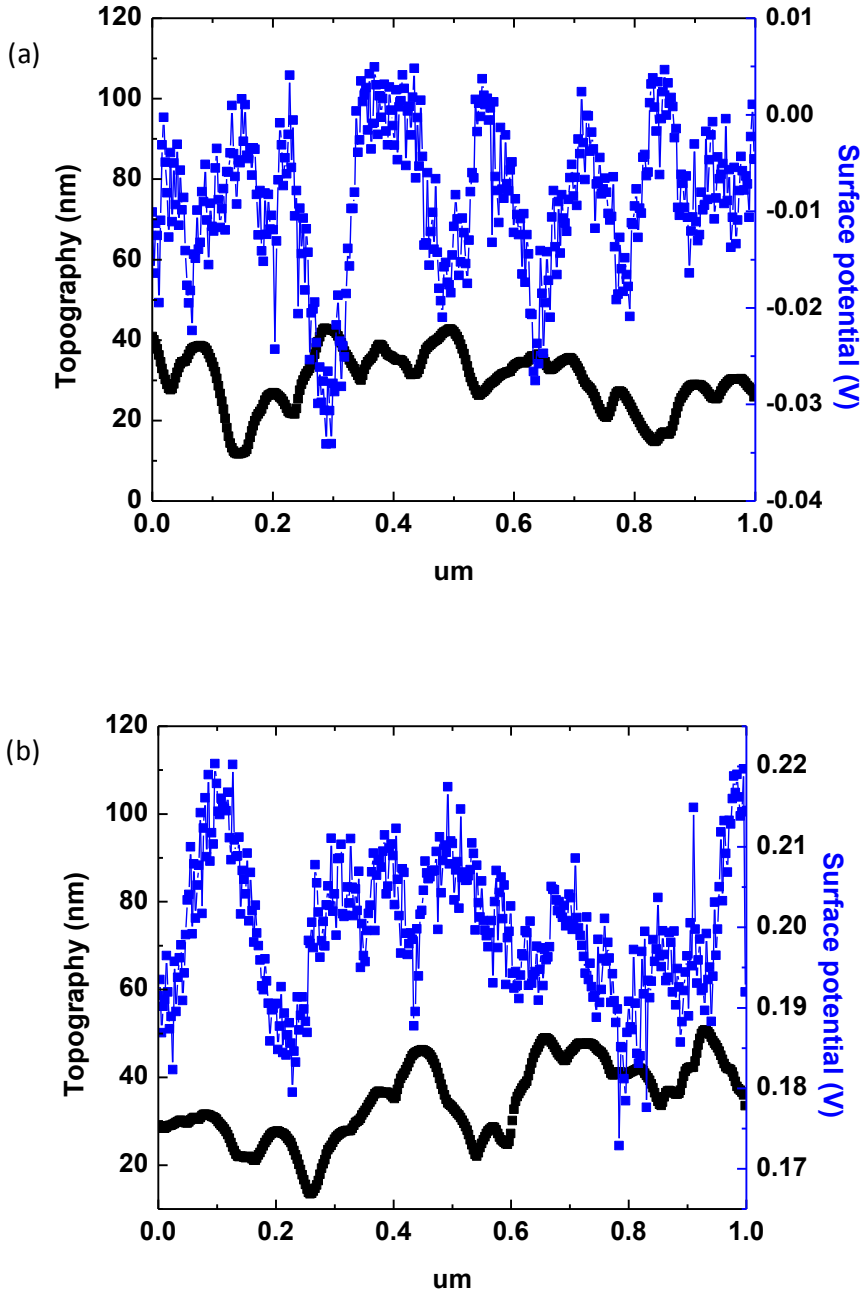

Figure 4.10 The line scanning profiles of topography and surface potential of (a) $CH_3NH_3SnI_3$ and (b) $CH_3NH_3PbI_3$ films, respectively.

To investigate the stability of $CH_3NH_3SnI_3$ absorber layer compared to $CH_3NH_3PbI_3$ counterpart, the comparative analysis was performed.

Figure 4.11 (b) shows the line profile conductivity extracted from AFM images under positive (+1V) of $CH_3NH_3PbI_3$. The conductivity measurements were taken right after the fabrication and after 24 hours. It can be observed that the current was decreased from 0.6 nano Amps at peaks down to 0.2 nano Amps at peaks. This means that the conductivity of the lead based film degraded within 24 hours. The sample was stored in nitrogen filled environment to eliminate the sample contact with oxygen and water molecules from ambient air environment. This indicated that the electrical properties of $CH_3NH_3PbI_3$ material are not stable and changes after the fabrication [27].

The similar behavior was observed for $CH_3NH_3SnI_3$ film as can be observed from Figure 4.11. The conductivity was decreased from 1 nano Amp at peaks down to 0.2 nano Amps at peaks within 24 hours. The $CH_3NH_3SnI_3$ sample was also kept in nitrogen environment to avoid exposure to ambient air. Similarly to $CH_3NH_3PbI_3$ counterpart, the electrical properties of $CH_3NH_3SnI_3$ material keep changing after the fabrication process without presence of oxygen and water molecules. This changes can be attributed either to the presence of nitrogen or internal chemical processes inside the material, or combination of both.

(a)

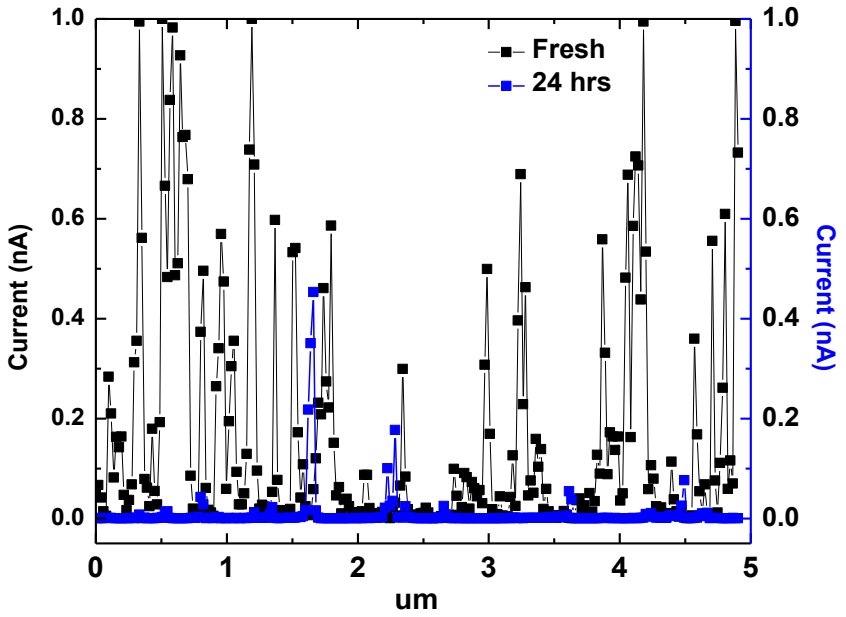

(b)

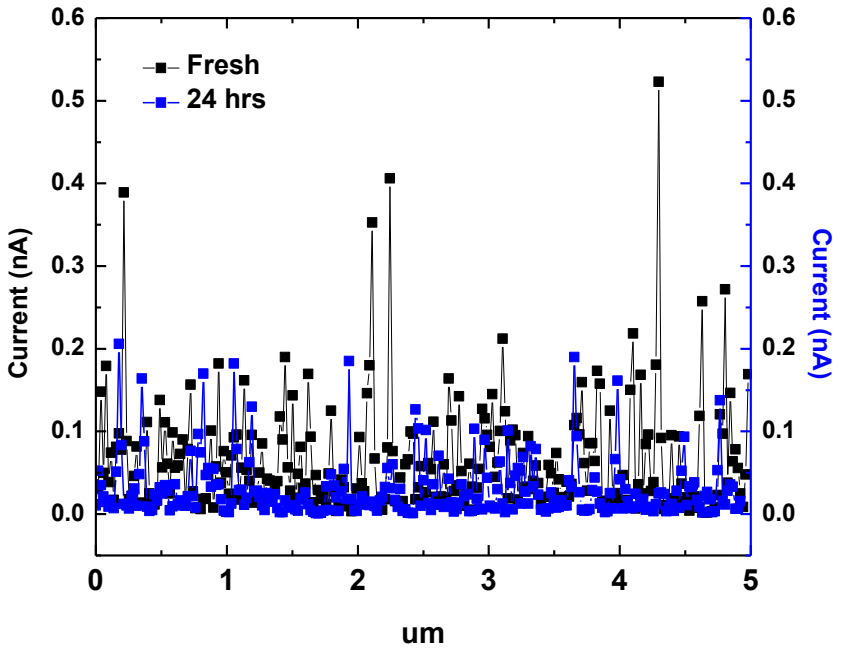

Figure 4.11 The line scanning profiles of the conductivity extracted from AFM images under positive (+1 V) of (a) $CH_3NH_3SnI_3$ and (b) $CH_3NH_3PbI_3$ films, respectively.

4.2 Electrical and morphological properties of $CH_3NH_3SnI_3$ film based on different preparation method

To investigate the material structure and purity, XRD measurements were performed. The diffraction patterns obtained in Figure 4.12 was in good agreement with literature data and corresponds to the perovskite structure type crystallized in the P4mm pseudocubic space group at ambient conditions [112]. It was investigated earlier that the crystal structure of $CH_3NH_3SnI_3$ transforms to a lower-symmetry tetragonal structure as observed for Pb analogue at low temperatures. This transition occurs through two stages at temperature of around 275 and 100 K [45]. The structure of $CH_3NH_3SnI_3$ is constructed of a network of corner sharing $[SnI_6]^{4-}$ polyhedra that encompass an organic cations, $[CH_3NH_3]^+$. It was noted that the organic monovalent cation $[CH_3NH_3]^+$ is highly disordered and free to rotate at high temperature because the thermal energy surpasses the energy barrier between different stable configurations[113, 114]. The distortion from the cubic (Pm-3m) structure occurs from orientational polarization of the $[CH_3NH_3]^+$ cations along the C-N bond direction. This distortion inflicts the three-dimensional [SnI3]- inorganic lattice [46]. It was also discussed that the organic $[CH_3NH_3]^+$ cations do not contribute to the formation of the valence band or the conduction band. They only play role in donating electrons [51].

The lattice constants for DFM and DMSO-GBL based compounds were calculated as 6.24 Å and 6.23 Å with the lattice strains of 0.0217 and 0.023, respectively. The volume average crystallite size of DMF based films was estimated at 27 nm, whereas that of DMSO-GBL based one was 25.4 nm. From the XRD plot in Figure 4.12, it can be clearly seen that DMF based $CH_3NH_3SnI_3$ film has higher intensities of the peaks at 14° (100) and

28° (200). This indicates that DMF based material has higher crystallinity compared to the DMSO-GBL based one, which was in agreement with the SEM analysis. The higher 14° and 28° peak intensities can be attributed to the crystalline platelets formed on the top of the surface shown in Figure 4.13.

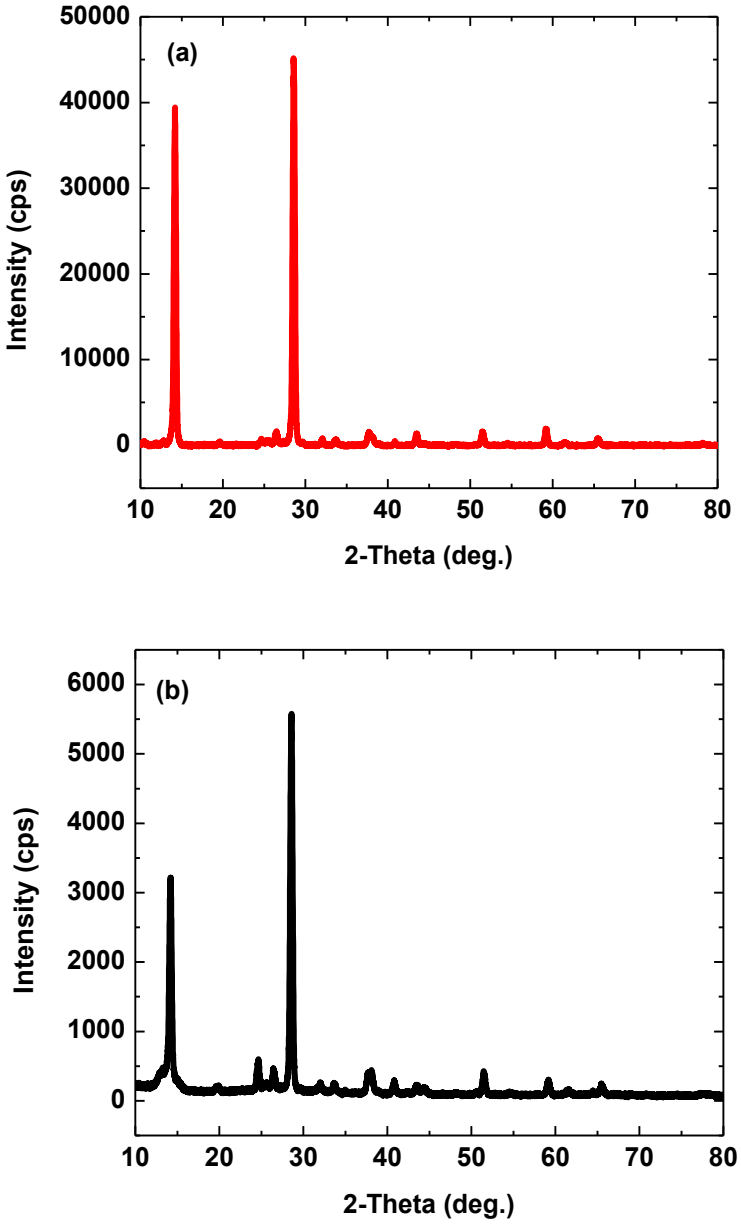

Figure 4.12 XRD spectra of $CH_3NH_3SnI_3$ processed from the (a) DMF and (b) DMSO-GBL solvents

Figure 4.13 shows SEM images of $CH_3NH_3SnI_3$ films spin-coated on mesoporous TiO_2 at 4500 rpm from (a) DMF and (b) DMSO-GBL solvents. The DMF based $CH_3NH_3SnI_3$ film show large randomly oriented cubic-like platelets with a size of ~ 15-20 µm. These platelets were formed on the top of the surface in addition to the $CH_3NH_3SnI_3$ that fills the pores of mesoporous TiO_2 [52]. The DMSO-GBL based $CH_3NH_3SnI_3$ film appears to be smooth and uniform with a small grain size. This suggests that film formation of $CH_3NH_3SnI_3$ can be controlled with precursor solvents.

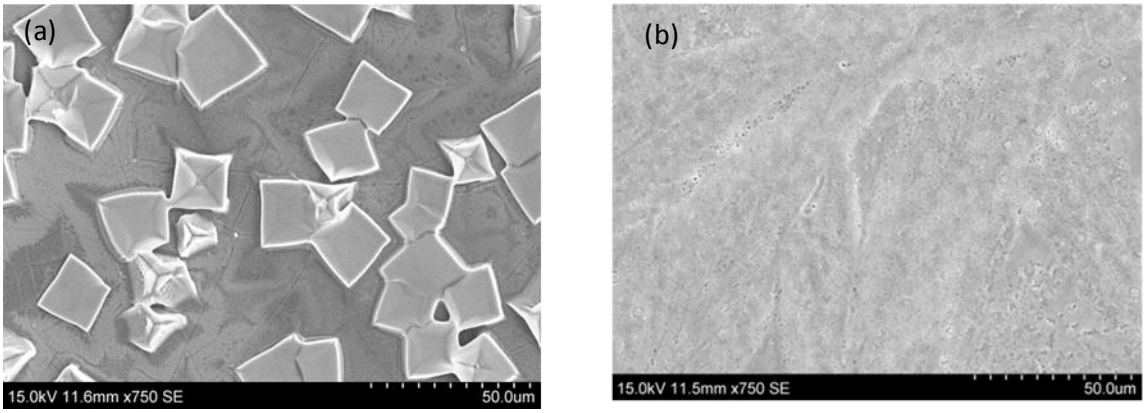

Figure 4.13 SEM images of $CH_3NH_3SnI_3$ films processed from (a) DMF and (b) DMSO-GBL solvents.

The optical properties of $CH_3NH_3SnI_3$ prepared from DMF and DMSO are shown in Figure 4.14. The optical absorption characteristics of $CH_3NH_3SnI_3$ material show broad absorption edge at approximately 950 nm. The optical bandgap of $CH_3NH_3SnI_3$ was estimated at 1.3 eV, which was in good agreement with literature [51, 52]. $CH_3NH_3SnI_3$ material showed higher absorption processed from DMF than that made from DMSO-GBL.

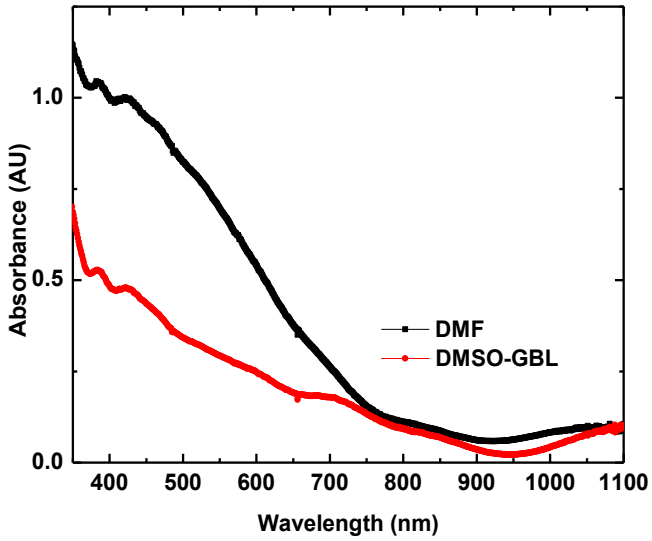

Figure 4.14 UV-Vis spectra of $CH_3NH_3SnI_3$ processed from DMF and DMSO-GBL, respectively.

The effects of morphology on photocurrent and nanoscale charge transport are also studied. Figure 4.15 shows a spatial topography map (2μm×2μm) of the surface of $CH_3NH_3SnI_3/TiO_2$/FTO/glass heterojunction structures based on DMF and DMSO-GBL, respectively. The grains varying in size between 20 and 200 nm were found in both structures. The DMF based film has higher surface roughness (Rrms = 1.85 nm) in contrast to DMSO-GBL film (Rrms = 0.68 nm). Comparing DMSO and GBL solvents, DMF has relatively lower boiling point (152°C) and higher saturated vapor pressure (2.7 Torr at 20°C). A lower boiling point and its corresponding higher evaporation rate resulted in a more rough film (Rrms = 1.85 nm). A comparative study with $CH_3NH_3SnI_3$ based on DMF and DMSO showed that DMSO solution derived $CH_3NH_3SnI_3$ perovskite films form ultrasmooth film, resulting in higher short-circuit photocurrent density [60]. On the contrary, other reports stated that rough surface with large grain size of perovskite film was a signature to the high light harvesting efficiency, which can reduce charge recombination

[115]. In order to find a correlation between short-circuit photocurrent and the morphology of $CH_3NH_3SnI_3$ perovskite, local photocurrent mapping of $CH_3NH_3SnI_3$ film using CS-AFM was performed.

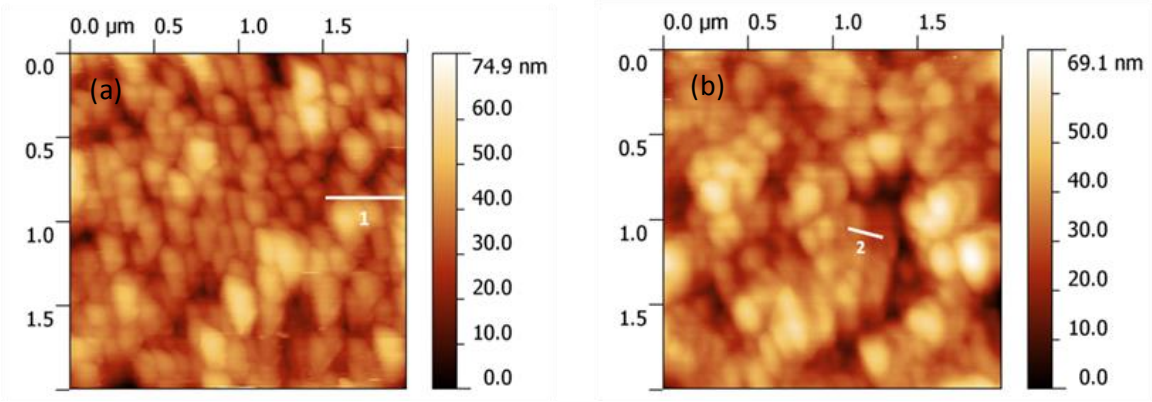

Figure 4.15 AFM topography images of $CH_3NH_3SnI_3$ films processed from (a) DMF and (b) DMSO-GBL solvents.

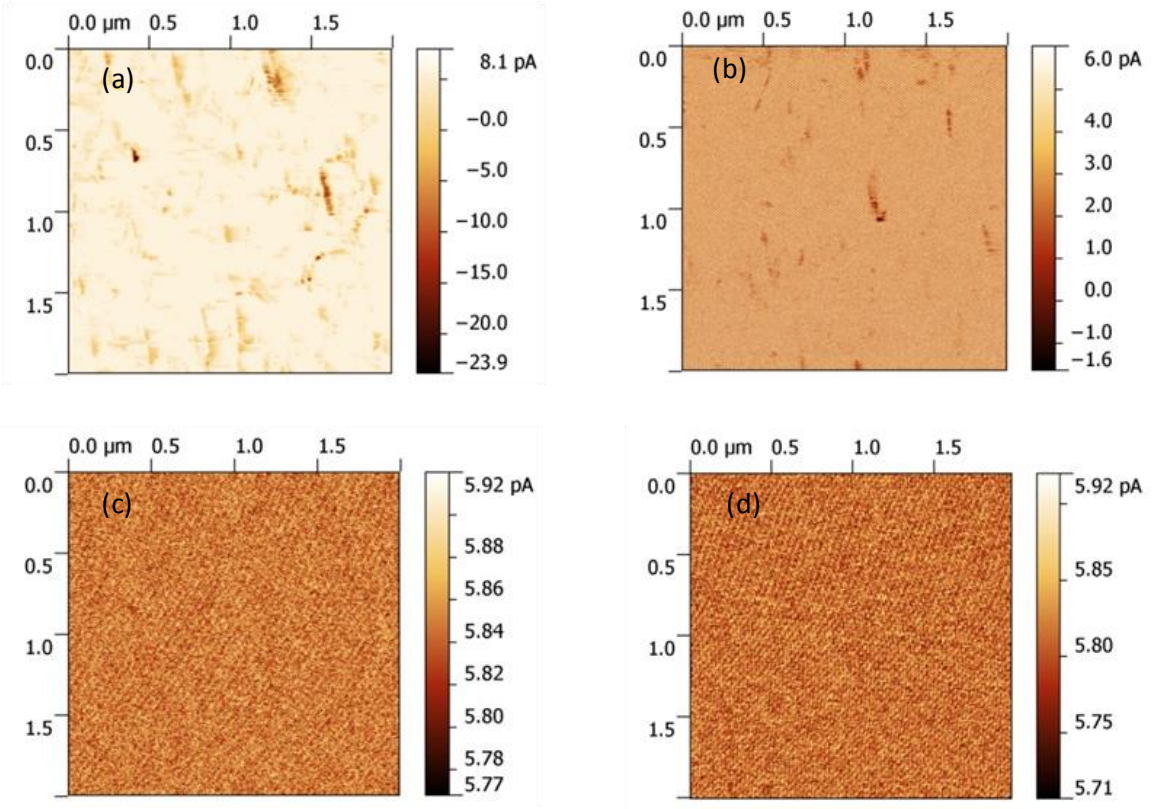

Figure 4.16 CS-AFM measurements performed on $CH_3NH_3SnI_3/TiO_2$/FTO/glass heterojunction structure: (a) photocurrent image under illumination for the sample made from DMF; (b) photocurrent image under illumination for the sample processed from DMSO-GBL; (c) current image taken in the dark at 0 V for the sample made from DMF; (d) current image taken in the dark at 0 V for the sample processed from DMF.

Photocurrent mapping of $CH_3NH_3SnI_3/TiO_2$/FTO/glass heterojunction structures made from DMF and DMSO-GBL are shown in Figure 4.16 (a) and (b), respectively. In the dark, there was no noticeable current observed in Figure 4.16(c) and (d), indicating a negligible effect of topography on current images. In the dark, the measured current was in the range of between 5.77 to 5.92 pA, which can be attributed to the background noise

of the instrument. When illuminated, the maximum photocurrent of $CH_3NH_3SnI_3$ based on DMF was ≈ -23.9 pA, whereas maximum in the DMSO-GBL film was ≈ -1pA. This indicates that the film $CH_3NH_3SnI_3$ based on DMF was capable to extract more excited charge carriers that can lead to higher photocurrent compared to the sample based on DMSO-GBL solvent. Even though the DMSO-GBL based sample has mush smooth and uniform film, the light harvesting capability is low compared to rough DMF based solvent with large sized grains. This confirms that crystalline thin film with large grains is signatures to a higher photocurrent density. The reason for low local photocurrent of DMSO-GBL can be attributed to low crystallinity of the film that can be extracted from XRD analysis.

Figure 4.17 shows a schematic of nanoscale charge injection and energy band diagram of $CH_3NH_3SnI_3$ [42]. Under illumination, the electrons were promoted from the valence band to the conduction band of $CH_3NH_3SnI_3$ film, transferred to TiO_2 and collected at the FTO electrode. The holes are collected by the Al tip, meaning that the current from CS-AFM measurements may be considered as a hole current. Since the direction of hole current under illumination was toward the tip, the measured values of the CS-AFM current have negative value. There was no capping layer or hole transport material deposited on top of $CH_3NH_3SnI_3$ film. Therefore, the $CH_3NH_3SnI_3$ surface was directly accessible by the AFM tip. Detailed sample preparation methods and CS-AFM measurements were described in the Experimental.

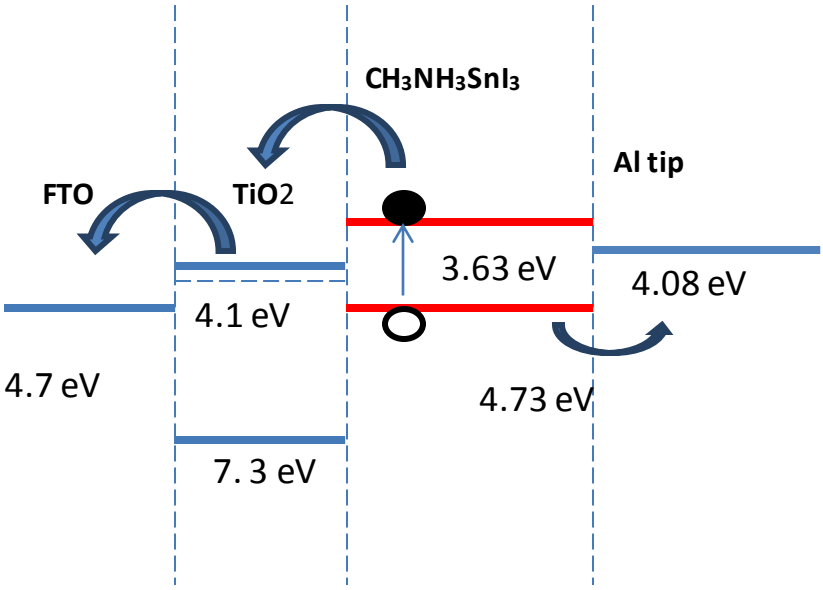

Figure 4.17 Band diagram showing charge collection of photocurrent of $CH_3NH_3SnI_3/TiO_2$/ FTO/glass heterojunction structure using Al-coated conductive tip.

Figure 4.18 shows a line topography profile of $CH_3NH_3SnI_3$ based on DFM and DMSO-GBL solvents used from topography AFM images depicted in

Figure 4.18. It was clear that the photocurrent was not evenly distributed over the surface of the film. Rather, the photocurrent was most prominent around grain boundaries (GBs). The photocurrent distribution maps of $CH_3NH_3SnI_3$ was in agreement with the current distribution of lead-based perovskites [28, 116]. It was earlier observed that the higher short-circuit current appears near GBs of $CH_3NH_3PbI_3$ rather than within grain interior [116]. The result showed that there was no direct correlation between the magnitude of the measured current and the height. For example, comparatively low local current was measured in the vicinity of GB2 where was a dip in the film morphology. Not all grain boundaries behave the same and were affected by crystallography and defect chemistry [117].

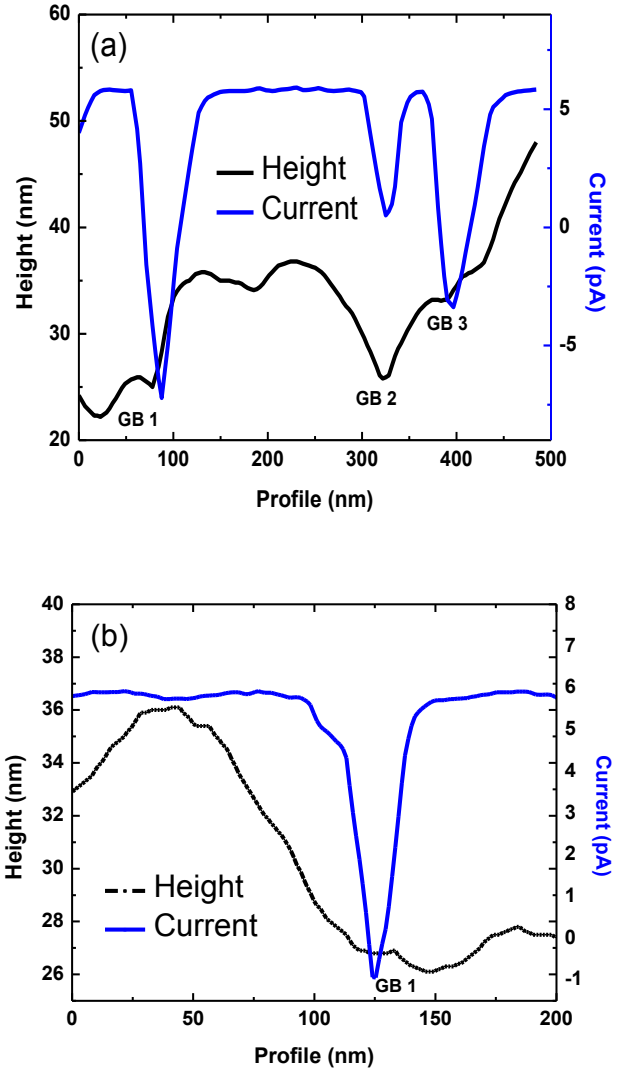

Figure 4.18 CS-AFM photocurrent and topography line profiles of $CH_3NH_3SnI_3$ processed from (a) DMF – line 1 on topography image and (b) DMSO-GBL solvents – line 2 on topography image, respectively.

Figure 4.19 shows maps of current distribution of DMF and DMSO-GBL based $CH_3NH_3SnI_3$ films under forward positive bias. When a forward bias (+1V) was applied on FTO electrode, the magnitude of CS-AFM current reaches up to 1nA for both films meaning that applied $CH_3NH_3SnI_3$ can be an electron transport material displaying metal-like conductivity. In some other reposts, $CH_3NH_3SnI_3$ was predicted to be better electron transporter than $CH_3NH_3PbI_3$ [48].

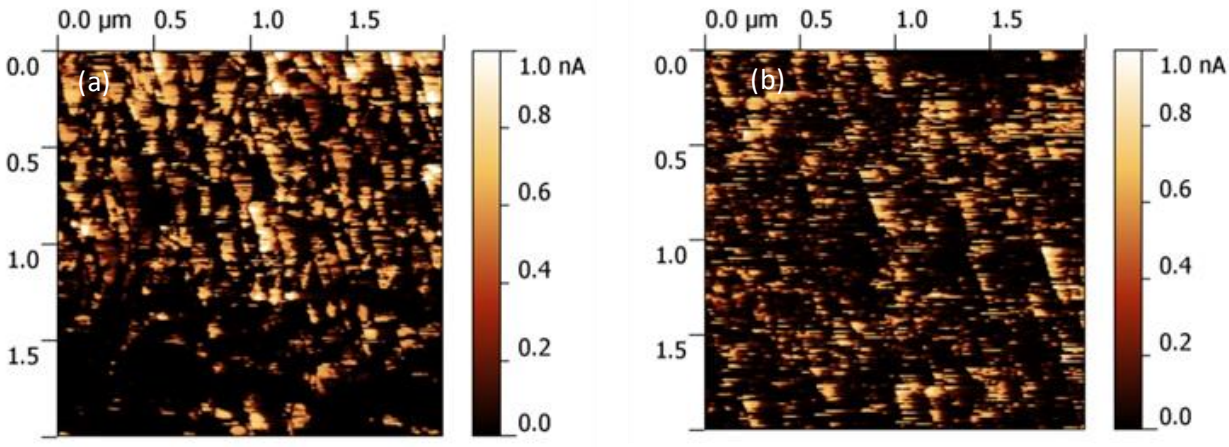

Figure 4.19 CS-AFM images of $CH_3NH_3SnI_3$ under positive (+1V) bias made from (a) DMF and (b) DMSO-GBL solvents, respectively.

Figure 4.20 represents CS-AFM images for $CH_3NH_3SnI_3$ samples based on DFM and DMSO-GBL when negative (-1V) bias applied. The images showed comparatively poor local current under negative polarity for both samples that can be attributed to the mismatch between Al tip and conduction band of $CH_3NH_3SnI_3$ meaning the poor collection of holes. This means that a small amount of holes can contribute to charge transport. This condition may be attributed to the diffusive behavior of the holes leading to the metallic charge transport [45].

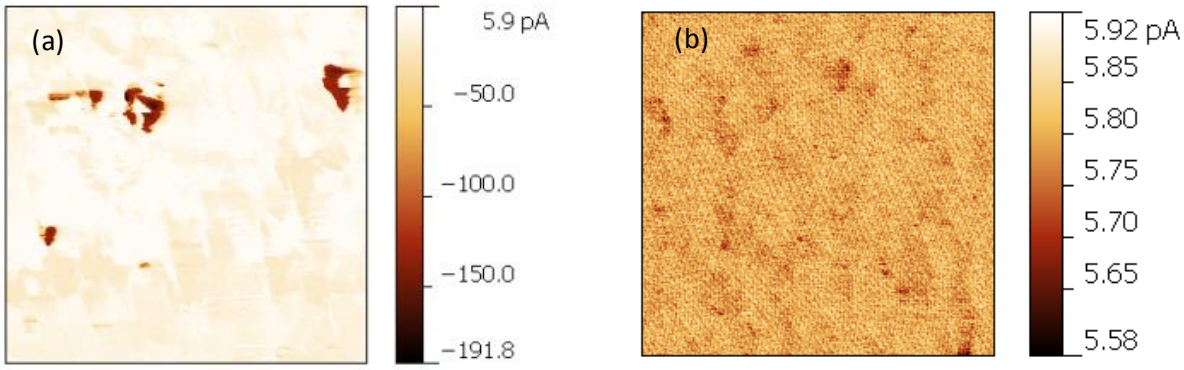

Figure 4.20 CS-AFM images of $CH_3NH_3SnI_3$ under negative (-1V) bias processed from (a) DMF and (b) DMSO-GBL solvents, respectively.

Figure 4.21 represents dark and illuminated local I-V plots of $CH_3NH_3SnI_3$ based on DMF and DMSO-GBL solvents. Local I-V spectroscopy was measured at single spots on the surface of $CH_3NH_3SnI_3$ film using CS-AFM technique to estimate charge carrier mobility. The conductive AFM tip was placed in the areas with high photocurrent observed from photocurrent CS-AFM images and the averaged I-V plot was used for calculations. A non-linear behavior of I-V plots advocates a non-Ohmic contact between the $CH_3NH_3SnI_3$ film and the tip [104, 118]. Moreover, both samples showed a quadratic dependence of local current with applied bias.

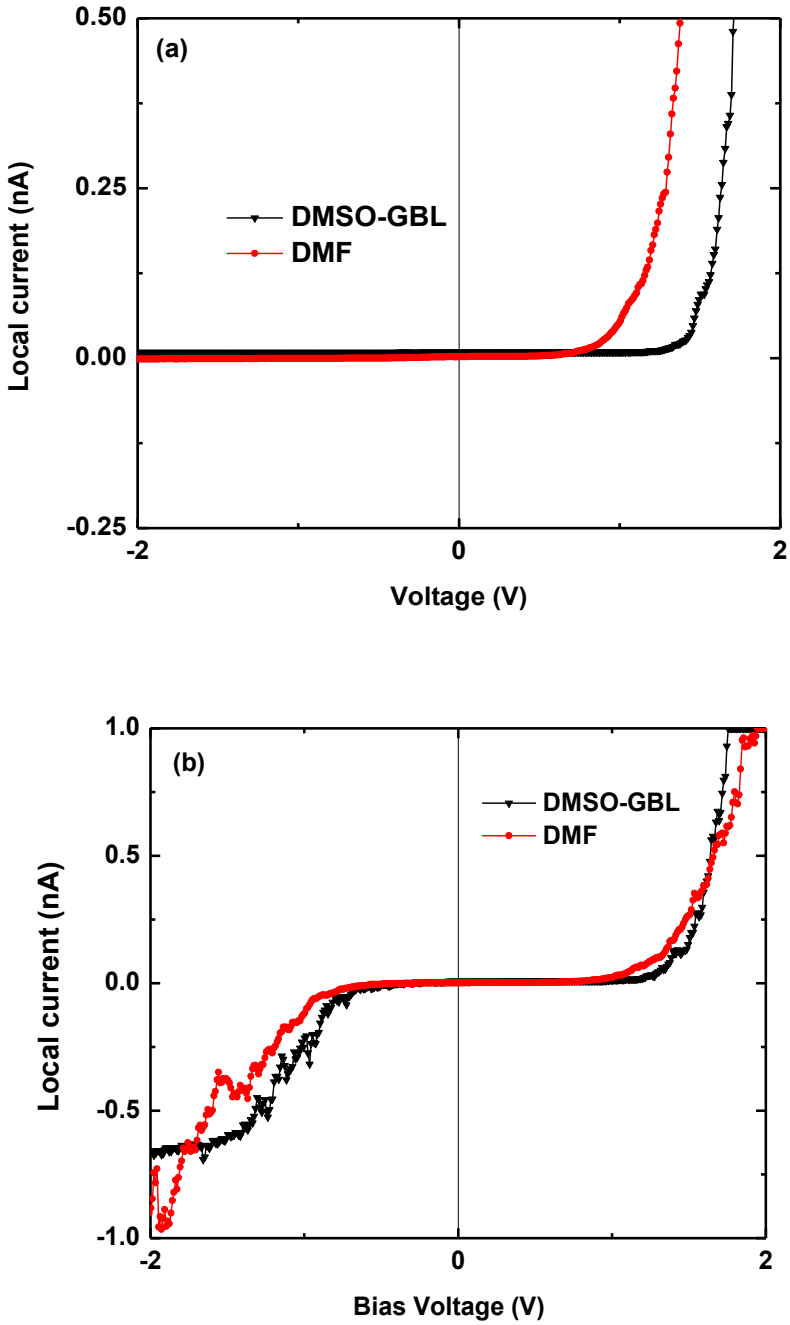

Figure 4.21 Local I-V dark (a) and illuminated (b) plots of $CH_3NH_3SnI_3$ processed from DMF and DMSO-GBL solvents, respectively.

The charge carrier mobility of $CH_3NH_3SnI_3$ based on DMF and DMSO-GBL solvents were calculated using the Space-Charge Limited Current model [104, 119, 120]. The charge carrier mobility was calculated as 0.59 $cm^2V^{-1}s^{-1}$ for DMF and 0.09 $cm^2V^{-1}s^{-1}$ for DMSO-GBL. The increase in carriers' mobility in DMF based sample may be attributed to the higher crystallinity of the film, allowing an efficient path for charge transport and improving charge collection. Figure 4.21 (b) shows a local current-voltage response under 0.5 kW/m^2 illumination. For both DFM and DMSO-GBL based samples, distinct kink of S-shape was observed in the forward bias under illumination, which was not observed in the dark I-V plots on Figure 4.21. A similar S-shape behavior of local I-V curves was reported for P3HT:PCBM under illumination, and not in the dark [60]. The absence of short circuit current in these plots can be attributed to an insufficient build-in electric field between the tip and the FTO electrode, resulting in poor collection of photogenerated charges by point-contact of the AFM tip at zero external bias.

Figure 4.22 shows photocurrent density-voltage (J-V) of $CH_3NH_3SnI_3$ solid state device based on DMF and DMSO-GBL solvents, respectively. Even though there was a broad spread in the performance of the $CH_3NH_3SnI_3$ solar cells, the solid state $CH_3NH_3SnI_3$ device based on DMF shows better efficiency of 0.36% with 0.16 V open circuit voltage compared to 0.24% efficiency with 0.1 V open circuit voltage of the $CH_3NH_3SnI_3$ solar cell based on DMSO-GBL. Fill factor was still as low as 0.28 for both devices.

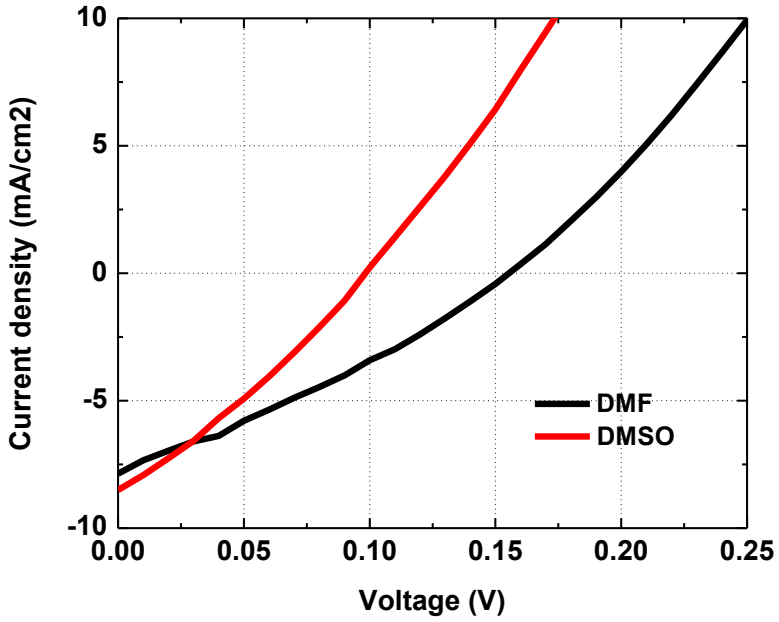

Figure 4.22 Photocurrent density-voltage (J-V) of $CH_3NH_3SnI_3$ solid state device based on DMF and DMSO-GBL solvents, respectively.

The slight increase of the efficiency for DMF based $CH_3NH_3SnI_3$ devices can be explained by higher crystallinity of the film. Nevertheless, the low fill factor can be an indication of high density of defects that can lead to high recombination rates for both devices. Low open circuit voltage can be explained by the fact that $CH_3NH_3SnI_3$ was a low bandgap (1.23 eV) semiconductor with metallic conductivity compared to 1.55 eV bandgap of $CH_3NH_3PbI_3$.

CHAPTER 5. CONCLUSIONS

5.1 Summary

For the last few years, perovskites such as methylammonium lead trihalide ($CH_3NH_3PbX_3$) have gained significant notice in photovoltaic application as a result of their low fabrication cost and high efficiency. The efficiency of devices using $CH_3NH_3PbX_3$ as an absorber material have increased dramatically from 3.9% in 2009 up to 22.1% in early 2016. One of the biggest concerns with this type of material is the toxicity of lead, which has potential to inflict damage upon both human and environment. The perovskite composites are salt-like minerals that dissolve easily in water. The prospect of dissolved lead from solar panels dripping onto the rooftops of homeowners can be a large obstacle for this technology being commercialized. Due to the anticipated toxicity from a potentially soluble lead source, lead needs to be replaced with other non-toxic elements.

There have been earlier attempts to fabricate lead free perovskite solar cells and investigate their material properties, their electrical and optical properties still remain uncertain. The understanding of correlation between morphological and electrical properties is opening the way to the design of lead free perovskite solar cells. Despite prosperous applications of the $CH_3NH_3SnI_3$ perovskite compound in photovoltaics, a systematic understanding of its electronic, optical, and electric properties is essential for further optimizing material properties.

There is a need to understand electrical, optical, and structural properties of $CH_3NH_3SnI_3$ perovskite material to make stable and high quality film for photovoltaic performance. The objective of this dissertation was to analyze electrical, optical, and structural properties of $CH_3NH_3SnI_3$ film to fabricate high quality film for photovoltaic

performance. The major novelty of this work is on analysis of morphological, electrical, and optical properties of $CH_3NH_3SnI_3$ perovskite material to understand the correlation between the morphology and light harvesting properties that can lead to better charge transport.

The term perovskite is derived from crystal structure with the general chemical formula exhibiting the stoichiometry as ABX_3, where A is an organic cation, B a divalent metal ion, and X an anion (O^{2-}, Cl^-, Br^-, I^-, or, in a few instances, S^{2-}), respectively, The photoanode of perovskite solar cell is composed of a thin mesoporous semiconducting layer (typically (TiO_2, Al_2O_3, etc.)) deposited on transparent conducting oxide glass substrate and coated with a layer of perovskite material. The role of perovskite material is to absorb the light, generate excited photoelectrons and to inject of the excited electrons into the TiO_2. The mesoporous TiO_2 layer provides a pathway for the injected electrons to move from perovskite layer to the transparent conducting substrate. The perovskite layer is sandwiched between the electron transport layer and hole transport layer. A hole transport layer is necessary for the charge separation and transport of holes from into the counter electrode. The counter electrode composed of silver deposited onto hole transport layer by thermal evaporation.

$CH_3NH_3SnI_3$ film was prepared with precursor solutions, equimolar quantities of CH_3NH_3I and SnI_2 with a concentration of 40 wt% was dissolved in DMF and DMSO-GBL with the ratio 3.5:7, respectively. The precursor solutions were spin coated onto TiO_2 coated substrates to form a dark-brown tin perovskite layer. To pinpoint the differences and similarities between lead based $CN_3NH_3PbI_3$ films and tin based $CH_3NH_3SnI_3$ counterparts, the comparative study was performed in terms of stability, morphological, and electrical properties of both thin films. An analytical study of optical and electrical properties of

$CH_3NH_3SnI_3$ films based on different solvents such as DMF and combination of DMSO with GBL was presented in this work. The surface morphology of the $CH_3NH_3SnI_3$ films were analyzed by SEM and AFM. The absorption of the fabricated $CH_3NH_3SnI_3$ films were measured by UV-VIS spectroscopy. XRD spectra, optical and morphological properties of $CH_3NH_3SnI_3$ film was conducted and correlated them with electrical properties using CS-AFM. $CH_3NH_3SnI_3$ solar cells were fabricated based on two different technics using DMF and DMSO-GBL solvents. The fabricated $CH_3NH_3SnI_3$ solar cells were tested using AM1.5 solar simulator at 100 mW/cm^2.

XRD analysis showed that 14°peaks are pretty similar for both tin and lead based perovskites. Peaks at 25°, 28°, 32°, 41°, and 43° can be attributed to $CH_3NH_3SnI_3$. The optical (UV-VIS) absorption of $CH_3NH_3SnI_3$ thin film showed broader absorption spectrum with absorption edge at approximately 1000 nm. $CH_3NH_3SnI_3$ may be a good electron transporter. However, in case of $CH_3NH_3SnI_3$ there is a tendency of towards oxidation which causes the material to be doped with Sn^{4+} thus behaving as p-type upon oxidation. DMF based material has higher crystallinity compared to the DMSO-GBL based one, which is in agreement with the SEM analysis. $CH_3NH_3SnI_3$ material showed higher absorption processed from DMF than that made from DMSO-GBL. CS-AFM showed that the photocurrent was not evenly distributed over the surface of the film. Rather, the photocurrent is most prominent around grain boundaries. The charge carrier mobility was calculated as 0.59 $cm^2V^{-1}s^{-1}$ for DMF and 0.09 $cm^2V^{-1}s^{-1}$ for DMSO-GBL. The increase in carriers' mobility in DMF based sample may be attributed to the higher crystallinity of the film, allowing an efficient path for charge transport and improving charge collection. Solid state $CH_3NH_3SnI_3$ device based on DMF shows better efficiency of 0.36% with 0.16 V

open circuit voltage compared to 0.24% efficiency with 0.1 V open circuit voltage of the $CH_3NH_3SnI_3$ solar cell based on DMSO-GBL. Fill factor was still low at 0.28 for both devices.

5.2 Conclusions

By summarizing and analyzing all the results of optical, electrical, and morphological measurements of $CH_3NH_3SnI_3$, it can be concluded that crystallization and film formation of $CH_3NH_3SnI_3$ can be controlled with precursor solvents. $CH_3NH_3SnI_3$ based on DMF has higher crystallinity and light harvesting capability compared to DMSO-GBL. Based on CS-AFM analysis and local current mapping, it was noticed that the photocurrent is most prominent around the grain boundaries for both samples. This is in agreement with photocurrent distribution for lead based perovskites. The increase in carrier mobility in DMF based sample may be attributed to the higher crystallinity of the film, allowing an efficient pathway for charge transport, thereby improving charge collection. The slight increase of the efficiency for DMF based $CH_3NH_3SnI_3$ devices can be explained by higher crystallinity of the film. Nevertheless, the low fill factor can be an indication of high density of defects that can lead to high recombination rates for both devices. Low open circuit voltage can be explained by the fact that $CH_3NH_3SnI_3$ is a low bandgap (1.23 eV) semiconductor with metal-like conductivity.

5.3 Future work

The efficiency of lead free perovskite solar cells can be achieved by improving the crystallinity of $CH_3NH_3SnI_3$ films and reducing the defects. Since $CH_3NH_3SnI_3$ crystalizes upon spin-coating at room temperature, the fabrication of $CH_3NH_3SnI_3$ films need to be

done below room temperature. The open circuit voltage can be improved by applying the right hole transport layer that enhances the separation of the excited charge carriers. The fermi level of hole transport material needs to match with the valence band of $CH_3NH_3SnI_3$ for efficient hole collection. The stability of $CH_3NH_3SnI_3$ still remains a challenge. Self-doping of $CH_3NH_3SnI_3$ upon oxidation must be suppressed in order to achieve stable, efficient, and non-toxic tin based solar cells.

SUPPLEMENTARY INFORMATION

Thermal Gravimetric Analysis of SnI_2

Thermal Gravimetric Analysis (TGA) was performed to ensure the stability of tin iodide (SnI_2) used for fabrication of $CH_3NH_3SnI_3$ thin films. TGA was performed under following conditions: N_2 flow rate of 20 mL/min, heating rate of 25C/min, and the temperature range from 25 C° to 900 Cº.

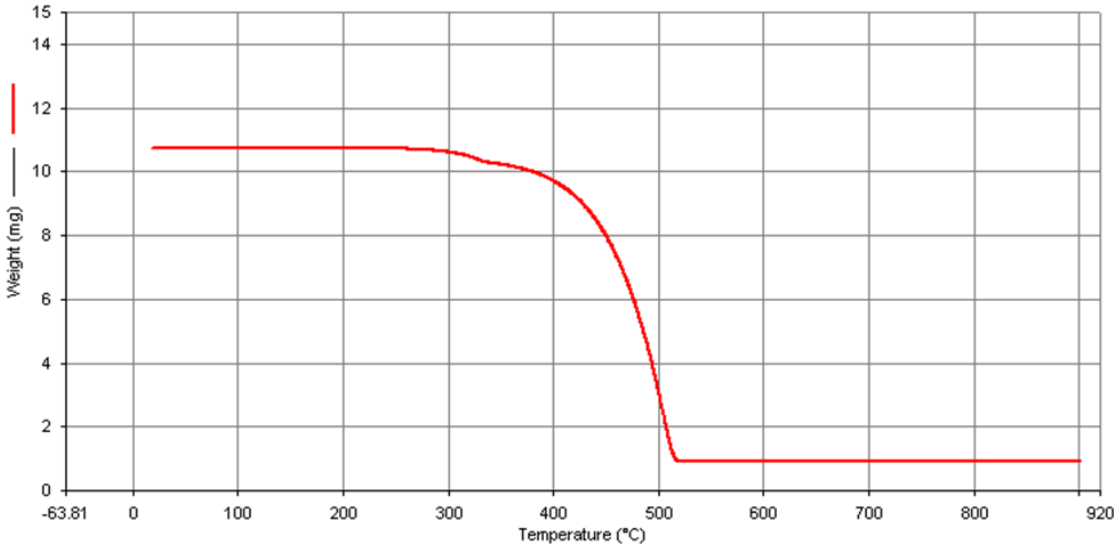

Figure S.1 Thermal Gravimetric Analysis of SnI_2

As evident from TGA curve in Figure S.1, SnI_2 weight does not change in the temperature range from 27 Cº to 270 C°. SnI_2 shows gradual weight loss starting at 270 Cº, which can be attributed either to the oxidation of SnI_2 to exposed air or to the melting of SnI_2 [43]. Since the fabrication of $CH_3NH_3SnI_3$ was performed at room temperature (27 C°), this indicates that SnI_2 was not oxidized and did not contained impurities.

Current Sensing Atomic Force Microscopy of sputtered gold

A demonstration sample of sputtered gold was tested to assure that the CS-AFM experimental setup was working as designed. The sample was prepared by sputtering deposition of gold film on silicon substrate. The thickness of deposited gold was 100 nm. Figure S.2 shows the topography (a) image and conductivity (CS-AFM) image taken by Agilent 5500 SPM in CS-AFM mode using 4-pin nose cone.

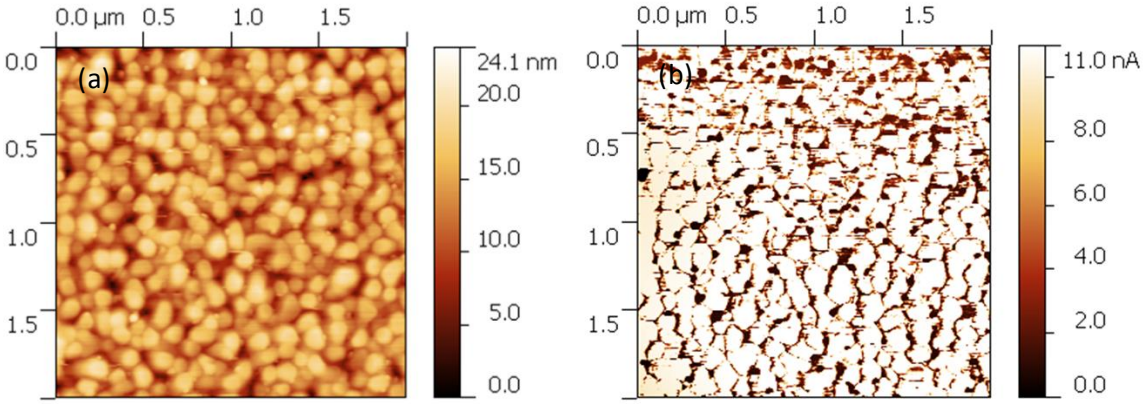

Figure S.2 The topography (a) and CS-AFM (b) images of sputtered gold thin film.

Since gold is a conductive material, by applying voltage bias to the sample, the electric current signal is expected. This test confirmed that CS-AFM experimental setup was in good working condition and the data obtained was accurate.

LITERATURE CITED

[1] R. A. Messenger and J. Ventre, *Photovoltaic systems engineering*: CRC, 2003.

[2] (2012). *How much carbon dioxide is produced by burning gasoline and diesel fuel?* Available: http://www.eia.gov/tools/faqs/faq.cfm?id=307&t=11

[3] O. Morton, "Solar energy: A new day dawning?: Silicon Valley sunrise," *Nature*, vol. 443, pp. 19-22, 2006.

[4] S. Bofinger and G. Heilscher, "Solar electricity forecast-approaches and first results," in *20th Europ. PV conf*, 2006.

[5] A. Hammer, "Documentation-EnMetSOL Satellite Data–Available Regions at Oldenburg University," Tech. rep., University of Oldenburg, available at: http://www. uni-oldenburg. de/fileadmin/user_upload/physik/ag/ehf/enmet/download/enmetsol-documentation. pdf(last access: 15 January 2016)2014.

[6] M. Schroedter-Homscheidt, C. Delamare, G. Heilscher, D. Heinemann, C. Hoyer, R. Meyer, *et al.*, "The ESA-ENVISOLAR project: experience on the commercial use of Earth observation based solar surface irradiance measurements for energy business purposes," *Solar Energy Resources management for Electricity Generation*, pp. 111-124, 2006.

[7] R. Gross, M. Leach, and A. Bauen, "Progress in renewable energy," *Environment International*, vol. 29, pp. 105-122, 2003.

[8] N. Gupta, G. Alapatt, R. Podila, R. Singh, and K. Poole, "Prospects of nanostructure-based solar cells for manufacturing future generations of photovoltaic modules," *International Journal of Photoenergy*, vol. 2009, 2009.

[9] M. A. Green, K. Emery, Y. Hishikawa, W. Warta, and E. D. Dunlop, "Solar cell efficiency tables (version 39)," *Progress in Photovoltaics: Research and Applications*, vol. 20, pp. 12-20, 2012.

[10] J. Zhao, A. Wang, M. A. Green, and F. Ferrazza, "19.8% efficient "honeycomb" textured multicrystalline and 24.4% monocrystalline silicon solar cells," *Applied Physics Letters*, vol. 73, pp. 1991-1993, 1998.

[11] M. A. Green, K. Emery, Y. Hishikawa, and W. Warta, "Solar cell efficiency tables (version 36)," *Progress in Photovoltaics: Research and Applications*, vol. 18, pp. 346-352, 2010.

[12] K. Kalyanasundaram, *Dye-sensitized solar cells*: CRC, 2009.

[13] N. G. Dhere, "Present status and future prospects of CIGSS thin film solar cells," *Solar energy materials and solar cells*, vol. 90, pp. 2181-2190, 2006.

[14] V. Aroutiounian, S. Petrosyan, A. Khachatryan, and K. Touryan, "Quantum dot solar cells," *Journal of Applied Physics*, vol. 89, pp. 2268-2271, 2001.

[15] C. Strümpel, M. McCann, G. Beaucarne, V. Arkhipov, A. Slaoui, V. Švrček, *et al.*, "Modifying the solar spectrum to enhance silicon solar cell efficiency—An overview of available materials," *Solar energy materials and solar cells*, vol. 91, pp. 238-249, 2007.

[16] S. Pillai and M. Green, "Plasmonics for photovoltaic applications," *Solar Energy Materials and Solar Cells*, vol. 94, pp. 1481-1486, 2010.

[17] M. Graetzel, R. A. Janssen, D. B. Mitzi, and E. H. Sargent, "Materials interface engineering for solution-processed photovoltaics," *Nature,* vol. 488, pp. 304-312, 2012.

[18] S. Sigdel, A. Dubey, H. Elbohy, A. Aboagye, D. Galipeau, L. Zhang, *et al.*, "Dye-sensitized solar cells based on spray-coated carbon nanofiber/TiO 2 nanoparticle composite counter electrodes," *Journal of Materials Chemistry A,* vol. 2, pp. 11448-11453, 2014.

[19] H. Elbohy, M. R. Kim, A. Dubey, K. M. Reza, D. Ma, J. Zai, *et al.*, "Incorporation of plasmonic Au nanostars into photoanodes for high efficiency dye-sensitized solar cells," *Journal of Materials Chemistry A,* vol. 4, pp. 545-551, 2016.

[20] S. Venkatesan, N. Adhikari, J. Chen, E. C. Ngo, A. Dubey, D. W. Galipeau, *et al.*, "Interplay of nanoscale domain purity and size on charge transport and recombination dynamics in polymer solar cells," *Nanoscale,* vol. 6, pp. 1011-1019, 2014.

[21] S. Venkatesan, E. C. Ngo, Q. Chen, A. Dubey, L. Mohammad, N. Adhikari, *et al.*, "Benzothiadiazole-based polymer for single and double junction solar cells with high open circuit voltage," *Nanoscale,* vol. 6, pp. 7093-7100, 2014.

[22] S. Venkatesan, Q. Chen, E. C. Ngo, N. Adhikari, K. Nelson, A. Dubey, *et al.*, "Polymer solar cells processed using anisole as a relatively nontoxic solvent," *Energy Technology,* vol. 2, pp. 269-274, 2014.

[23] D. Khatiwada, S. Venkatesan, J. Chen, Q. Chen, N. Adhikari, A. Dubey, *et al.*, "Morphological evolution and its impacts on performance of polymer solar cells," *IEEE Transactions on Electron Devices,* vol. 62, pp. 1284-1290, 2015.

[24] D. Khatiwada, S. Venkatesan, Q. Chen, J. Chen, N. Adhikari, A. Dubey, *et al.*, "Improved performance by morphology control via fullerenes in PBDT-TBT-alkoBT based organic solar cells," *Journal of Materials Chemistry A,* vol. 3, pp. 15307-15313, 2015.

[25] A. F. Mitul, L. Mohammad, B. Vaagensmith, A. Dubey, D. Khatiwada, and Q. Qiao, "Optimization of Interconnecting Layers for Double-and Triple-Junction Polymer Solar Cells," *IEEE Journal of Photovoltaics,* vol. 5, pp. 1674-1679, 2015.

[26] A. F. Mitul, L. Mohammad, B. Vaagensmith, D. Khatiwada, A. Dubey, and Q. Qiao, "Optimization of interfacial layer for double and triple junction polymer solar cell," in *SPIE Organic Photonics+ Electronics,* 2015, pp. 95671R-95671R-3.

[27] A. Dubey, N. Adhikari, S. Venkatesan, S. Gu, D. Khatiwada, Q. Wang, *et al.*, "Solution processed pristine PDPP3T polymer as hole transport layer for efficient perovskite solar cells with slower degradation," *Solar Energy Materials and Solar Cells,* vol. 145, pp. 193-199, 2016.

[28] N. Adhikari, A. Dubey, D. Khatiwada, A. F. Mitul, Q. Wang, S. Venkatesan, *et al.*, "Interfacial study to suppress charge carrier recombination for high efficiency Perovskite solar cells," *ACS applied materials & interfaces,* 2015.

[29] D. Khatiwada, S. Venkatesan, N. Adhikari, A. Dubey, A. F. Mitul, L. Mohammad, *et al.*, "Efficient Perovskite Solar Cells by Temperature Control in Single and Mixed Halide Precursor Solutions and Films," *The Journal of Physical Chemistry C*, vol. 119, pp. 25747-25753, 2015.

[30] N. Adhikari, A. Dubey, E. A. Gaml, B. Vaagensmith, K. M. Reza, S. A. A. Mabrouk, *et al.*, "Crystallization of a perovskite film for higher performance solar cells by controlling water concentration in methyl ammonium iodide precursor solution," *Nanoscale*, vol. 8, pp. 2693-2703, 2016.

[31] A. Dubey, N. Adhikari, S. Venkatesan, S. Gu, D. Khatiwada, Q. Wang, *et al.*, "Shelf life stability comparison in air for solution processed pristine PDPP3T polymer and doped spiro-OMeTAD as hole transport layer for perovskite solar cell," *Data in Brief*, vol. 7, pp. 139-142, 2016.

[32] A. Kojima, K. Teshima, Y. Shirai, and T. Miyasaka, "Organometal halide perovskites as visible-light sensitizers for photovoltaic cells," *Journal of the American Chemical Society*, vol. 131, pp. 6050-6051, 2009.

[33] G. E. Eperon, V. M. Burlakov, P. Docampo, A. Goriely, and H. J. Snaith, "Morphological Control for High Performance, Solution-Processed Planar Heterojunction Perovskite Solar Cells," *Advanced Functional Materials*, vol. 24, pp. 151-157, 2014.

[34] H.-S. Kim, C.-R. Lee, J.-H. Im, K.-B. Lee, T. Moehl, A. Marchioro, *et al.*, "Lead iodide perovskite sensitized all-solid-state submicron thin film mesoscopic solar cell with efficiency exceeding 9%," *Scientific reports*, vol. 2, 2012.

[35] G. Hodes, "Perovskite-based solar cells," *Science*, vol. 342, pp. 317-318, 2013.

[36] M. Liu, M. B. Johnston, and H. J. Snaith, "Efficient planar heterojunction perovskite solar cells by vapour deposition," *Nature,* vol. 501, pp. 395-398, 2013.

[37] J. Burschka, N. Pellet, S.-J. Moon, R. Humphry-Baker, P. Gao, M. K. Nazeeruddin, *et al.*, "Sequential deposition as a route to high-performance perovskite-sensitized solar cells," *Nature,* vol. 499, pp. 316-319, 2013.

[38] N.-G. Park, "Organometal perovskite light absorbers toward a 20% efficiency low-cost solid-state mesoscopic solar cell," *The Journal of Physical Chemistry Letters,* vol. 4, pp. 2423-2429, 2013.

[39] V. Gonzalez-Pedro, E. J. Juarez-Perez, W.-S. Arsyad, E. M. Barea, F. Fabregat-Santiago, I. Mora-Sero, *et al.*, "General working principles of CH3NH3PbX3 perovskite solar cells," *Nano letters,* vol. 14, pp. 888-893, 2014.

[40] V. T. Breslin and S. A. Sañudo-Wilhelmy, "The lead project. An environmental instrumental analysis case study," *J. Chem. Educ,* vol. 78, p. 1647, 2001.

[41] B. P. Lanphear, T. D. Matte, J. Rogers, R. P. Clickner, B. Dietz, R. L. Bornschein, *et al.*, "The contribution of lead-contaminated house dust and residential soil to children's blood lead levels: a pooled analysis of 12 epidemiologic studies," *Environmental research,* vol. 79, pp. 51-68, 1998.

[42] P. Gao, M. Grätzel, and M. K. Nazeeruddin, "Organohalide lead perovskites for photovoltaic applications," *Energy & Environmental Science,* vol. 7, pp. 2448-2463, 2014.

[43] F. Hao, C. C. Stoumpos, D. H. Cao, R. P. Chang, and M. G. Kanatzidis, "Lead-free solid-state organic-inorganic halide perovskite solar cells," *Nature Photonics,* vol. 8, pp. 489-494, 2014.

[44] D. B. Mitzi, C. Feild, Z. Schlesinger, and R. Laibowitz, "Transport, optical, and magnetic properties of the conducting halide perovskite CH3NH3SnI3," *Journal of Solid State Chemistry,* vol. 114, pp. 159-163, 1995.

[45] Y. Takahashi, R. Obara, Z.-Z. Lin, Y. Takahashi, T. Naito, T. Inabe, *et al.*, "Charge-transport in tin-iodide perovskite CH 3 NH 3 SnI 3: origin of high conductivity," *Dalton Transactions,* vol. 40, pp. 5563-5568, 2011.

[46] C. C. Stoumpos, C. D. Malliakas, and M. G. Kanatzidis, "Semiconducting tin and lead iodide perovskites with organic cations: phase transitions, high mobilities, and near-infrared photoluminescent properties," *Inorganic chemistry,* vol. 52, pp. 9019-9038, 2013.

[47] T. Yokoyama, D. H. Cao, C. C. Stoumpos, T.-B. Song, Y. Sato, S. Aramaki, *et al.*, "Overcoming Short-Circuit in Lead-Free CH3NH3SnI3 Perovskite Solar Cells via Kinetically Controlled Gas–Solid Reaction Film Fabrication Process," *The journal of physical chemistry letters,* vol. 7, pp. 776-782, 2016.

[48] P. Umari, E. Mosconi, and F. De Angelis, "Relativistic GW calculations on CH3NH3PbI3 and CH3NH3SnI3 perovskites for solar cell applications," *Scientific reports,* vol. 4, 2014.

[49] J. Im, C. C. Stoumpos, H. Jin, A. J. Freeman, and M. G. Kanatzidis, "Antagonism between Spin–Orbit Coupling and Steric Effects Causes Anomalous Band Gap Evolution in the Perovskite Photovoltaic Materials CH3NH3Sn1–x Pb x I3," *The Journal of Physical Chemistry Letters,* vol. 6, pp. 3503-3509, 2015.

[50] C. Kagan, D. Mitzi, and C. Dimitrakopoulos, "Organic-inorganic hybrid materials as semiconducting channels in thin-film field-effect transistors," *Science*, vol. 286, pp. 945-947, 1999.

[51] C. Bernal and K. Yang, "First-principles hybrid functional study of the organic–inorganic perovskites CH3NH3SnBr3 and CH3NH3SnI3," *The Journal of Physical Chemistry C*, vol. 118, pp. 24383-24388, 2014.

[52] N. K. Noel, S. D. Stranks, A. Abate, C. Wehrenfennig, S. Guarnera, A.-A. Haghighirad, *et al.*, "Lead-free organic–inorganic tin halide perovskites for photovoltaic applications," *Energy & Environmental Science*, vol. 7, pp. 3061-3068, 2014.

[53] J. Nelson, *The physics of solar cells* vol. 1: World Scientific, 2003.

[54] D. F. Marrón, A. Meeder, S. Sadewasser, R. Würz, C. Kaufmann, T. Glatzel, *et al.*, "Lift-off process and rear-side characterization of CuGaSe2 chalcopyrite thin films and solar cells," *Journal of applied physics*, vol. 97, p. 094915, 2005.

[55] M. M. Lee, J. Teuscher, T. Miyasaka, T. N. Murakami, and H. J. Snaith, "Efficient hybrid solar cells based on meso-superstructured organometal halide perovskites," *Science*, vol. 338, pp. 643-647, 2012.

[56] L. K. NREL, "Best Research-Cell Efficiencies," ed.

[57] M. A. Green, "Corrigendum to ‘Solar cell efficiency tables (version 46)’[Prog. Photovolt: Res. Appl. 2015; 23: 805–812]," *Progress in Photovoltaics: Research and Applications*, vol. 23, pp. 1202-1202, 2015.

[58] N. Adhikari, D. Khatiwada, A. Dubey, and Q. Qiao, "Device and morphological engineering of organic solar cells for enhanced charge transport and photovoltaic performance," *Journal of Photonics for Energy*, vol. 5, pp. 057207-057207, 2015.

[59] A. F. Mitul, L. Mohammad, S. Venkatesan, N. Adhikari, S. Sigdel, Q. Wang, *et al.*, "Low temperature efficient interconnecting layer for tandem polymer solar cells," *Nano Energy*, vol. 11, pp. 56-63, 2015.

[60] F. Hao, C. C. Stoumpos, P. Guo, N. Zhou, T. J. Marks, R. P. Chang, *et al.*, "Solvent-Mediated Crystallization of CH3NH3SnI3 Films for Heterojunction Depleted Perovskite Solar Cells," *Journal of the American Chemical Society*, vol. 137, pp. 11445-11452, 2015.

[61] J. Nelson, *The physics of solar cell*. Singapore: Imperial College Press, 2003.

[62] M. Johnsson and P. Lemmens, "Crystallography and chemistry of perovskites," *Handbook of magnetism and advanced magnetic materials*, 2007.

[63] S. Stølen, E. Bakken, and C. E. Mohn, "Oxygen-deficient perovskites: linking structure, energetics and ion transport," *Physical Chemistry Chemical Physics*, vol. 8, pp. 429-447, 2006.

[64] E. J. Juarez-Perez, R. S. Sanchez, L. Badia, G. Garcia-Belmonte, Y. S. Kang, I. Mora-Sero, *et al.*, "Photoinduced giant dielectric constant in lead halide perovskite solar cells," *The journal of physical chemistry letters*, vol. 5, pp. 2390-2394, 2014.

[65] A. K. Batra, S. Bhattacharjee, A. K. Chilvery, M. D. Aggarwal, M. E. Edwards, and A. Bhalla, "Simulation of energy harvesting from roads via pyroelectricity," *Journal of Photonics for Energy*, vol. 1, pp. 014001-014001-12, 2011.

[66] D. B. Mitzi, "Synthesis, structure, and properties of organic-inorganic perovskites and related materials," *Progress in Inorganic Chemistry, Volume 48*, pp. 1-121, 2007.

[67] H.-S. Kim, S. H. Im, and N.-G. Park, "Organolead halide perovskite: New horizons in solar cell research," *The Journal of Physical Chemistry C*, vol. 118, pp. 5615-5625, 2014.

[68] M. A. Loi and J. C. Hummelen, "Hybrid solar cells: perovskites under the sun," *Nature materials*, vol. 12, pp. 1087-1089, 2013.

[69] J. M. Frost, K. T. Butler, F. Brivio, C. H. Hendon, M. Van Schilfgaarde, and A. Walsh, "Atomistic origins of high-performance in hybrid halide perovskite solar cells," *Nano letters*, vol. 14, pp. 2584-2590, 2014.

[70] D. B. Mitzi, C. Feild, W. Harrison, and A. Guloy, "Conducting tin halides with a layered organic-based perovskite structure," 1994.

[71] R. S. Roth, "Classification of perovskite and other ABO3-type compounds," *J. Res. Nat. Bur. Stand*, vol. 58, pp. 75-88, 1957.

[72] D. B. Mitzi, "Templating and structural engineering in organic–inorganic perovskites," *Journal of the Chemical Society, Dalton Transactions*, pp. 1-12, 2001.

[73] D. B. Mitzi, K. Chondroudis, and C. R. Kagan, "Organic-inorganic electronics," *IBM journal of research and development*, vol. 45, pp. 29-45, 2001.

[74] I. Koutselas, L. Ducasse, and G. C. Papavassiliou, "Electronic properties of three- and low-dimensional semiconducting materials with Pb halide and Sn halide units," *Journal of Physics: Condensed Matter*, vol. 8, p. 1217, 1996.

[75] J. L. Knutson, J. D. Martin, and D. B. Mitzi, "Tuning the band gap in hybrid tin iodide perovskite semiconductors using structural templating," *Inorganic chemistry,* vol. 44, pp. 4699-4705, 2005.

[76] X. Zhou, F. P. Doty, and P. Yang, "Atomistic models for scintillator discovery," in *SPIE Optical Engineering+ Applications*, 2010, pp. 78060E-78060E-6.

[77] V. M. Goldschmidt, *Geochemische Verteilungsgesetze der Elemente*: Det Norske videnskaps-akademi, 1938.

[78] A. Poglitsch and D. Weber, "Dynamic disorder in methylammoniumtrihalogenoplumbates (II) observed by millimeter-wave spectroscopy," *The Journal of chemical physics,* vol. 87, pp. 6373-6378, 1987.

[79] N. Gippius, E. Muljarov, S. Tikhodeev, T. Ishihara, and L. Keldysh, "Dielectrically confined excitons and polaritons in natural superlattices-perovskite lead iodide semiconductors," in *MRS Proceedings*, 1993, p. 775.

[80] S. A. Bretschneider, J. Weickert, J. A. Dorman, and L. Schmidt-Mende, "Research update: physical and electrical characteristics of lead halide perovskites for solar cell applications," *APL Materials,* vol. 2, p. 040701, 2014.

[81] D.-J. Kwak, B.-H. Moon, D.-K. Lee, C.-S. Park, and Y.-M. Sung, "Comparison of transparent conductive indium tin oxide, titanium-doped indium oxide, and fluorine-doped tin oxide films for dye-sensitized solar cell application," *Journal of Electrical Engineering and Technology,* vol. 6, pp. 684-687, 2011.

[82] L. Sun, "Perovskite solar cells: Crystal crosslinking," *Nature chemistry,* 2015.

[83] E. Hendry, M. Koeberg, B. O'regan, and M. Bonn, "Local field effects on electron transport in nanostructured TiO2 revealed by terahertz spectroscopy," *Nano letters*, vol. 6, pp. 755-759, 2006.

[84] G. Yang, H. Tao, P. Qin, W. Ke, and G. Fang, "Recent progress in electron transport layers for efficient perovskite solar cells," *Journal of Materials Chemistry A*, vol. 4, pp. 3970-3990, 2016.

[85] A. G. Milnes, *Heterojunctions and metal semiconductor junctions*: Elsevier, 2012.

[86] D.-H. Do, "Investigation of ferroelectricity and piezoelectricity in ferroelectric thin film capacitors using synchrotron X-ray microdiffraction," 2006.

[87] J. I. Langford and A. Wilson, "Scherrer after sixty years: a survey and some new results in the determination of crystallite size," *Journal of Applied Crystallography*, vol. 11, pp. 102-113, 1978.

[88] J. Goldstein, D. E. Newbury, P. Echlin, D. C. Joy, A. D. Romig Jr, C. E. Lyman, *et al., Scanning electron microscopy and X-ray microanalysis: a text for biologists, materials scientists, and geologists*: Springer Science & Business Media, 2012.

[89] F. Krumeick, "Properties of electrons, their interactions with matter and applications in electron microscopy," *Laboratory of Inorganic Chemistry, disponível em http://www. microscopy. ethz. ch/downloads/Interactions. pdf, consultado em*, pp. 3-08, 2011.

[90] N. Maeda and T. J. Senden, "A method for the calibration of force microscopy cantilevers via hydrodynamic drag," *Langmuir*, vol. 16, pp. 9282-9286, 2000.

[91] S. K. Ramdon, "Nanoscale Characterization of Aged Li-Ion Battery Cathodes," The Ohio State University, 2013.

[92] T. Pompe, A. Fery, and S. Herminghaus, "Imaging liquid structures on inhomogeneous surfaces by scanning force microscopy," *Langmuir*, vol. 14, pp. 2585-2588, 1998.

[93] R. Magerle, "Nanotomography," *Physical review letters*, vol. 85, p. 2749, 2000.

[94] C. A. Putman, K. O. Van der Werf, B. G. De Grooth, N. F. Van Hulst, and J. Greve, "Tapping mode atomic force microscopy in liquid," *Applied physics letters*, vol. 64, pp. 2454-2456, 1994.

[95] M. Freitag, M. Radosavljević, W. Clauss, and A. Johnson, "Local electronic properties of single-wall nanotube circuits measured by conducting-tip AFM," *Physical Review B*, vol. 62, p. R2307, 2000.

[96] W. Melitz, J. Shen, A. C. Kummel, and S. Lee, "Kelvin probe force microscopy and its application," *Surface Science Reports*, vol. 66, pp. 1-27, 2011.

[97] M. Yasutake, D. Aoki, and M. Fujihira, "Surface potential measurements using the Kelvin probe force microscope," *Thin Solid Films*, vol. 273, pp. 279-283, 1996.

[98] L. Liu and G. Li, "Electrical characterization of single-walled carbon nanotubes in organic solar cells by Kelvin probe force microscopy," *Applied Physics Letters*, vol. 96, p. 083302, 2010.

[99] S. Sadewasser, T. Glatzel, R. Shikler, Y. Rosenwaks, and M. C. Lux-Steiner, "Resolution of Kelvin probe force microscopy in ultrahigh vacuum: comparison

of experiment and simulation," *Applied Surface Science,* vol. 210, pp. 32-36, 2003.

[100] R. Wiesendanger, *Scanning probe microscopy and spectroscopy: methods and applications*: Cambridge University Press, 1994.

[101] J. Millán, P. Godignon, and A. Pérez-Tomás, "Wide band gap semiconductor devices for power electronics," *Automatika–Journal for Control, Measurement, Electronics, Computing and Communications,* vol. 53, 2012.

[102] A. Cowley and S. Sze, "Surface states and barrier height of metal-semiconductor systems," *Journal of Applied Physics,* vol. 36, pp. 3212-3220, 1965.

[103] P. Stallinga, "Electrical characterization of organic (amorphous) electronic materials," *physica status solidi (c),* vol. 11, pp. 1389-1392, 2014.

[104] O. G. Reid, K. Munechika, and D. S. Ginger, "Space charge limited current measurements on conjugated polymer films using conductive atomic force microscopy," *Nano letters,* vol. 8, pp. 1602-1609, 2008.

[105] D. Braga, N. Battaglini, A. Yassar, G. Horowitz, M. Campione, A. Sassella, *et al.*, "Bulk electrical properties of rubrene single crystals: Measurements and analysis," *Physical review B,* vol. 77, p. 115205, 2008.

[106] W. Chandra, L. Ang, K. Pey, and C. Ng, "Two-dimensional analytical Mott-Gurney law for a trap-filled solid," *Applied physics letters,* vol. 90, p. 153505, 2007.

[107] S. Ghanavi, "Organic-inorganic hybrid perovskites as light absorbing/hole conducting material in solar cells," Master Thesis 30 hp vt 2013, UPPSALA Universitet, Stockholm Arlanda, 2013.

[108] W.-J. Yin, T. Shi, and Y. Yan, "Unusual defect physics in CH3NH3PbI3 perovskite solar cell absorber," *Applied Physics Letters*, vol. 104, p. 063903, 2014.

[109] B. Liu, W. Zhu, Y. Wang, W. Wu, X. Li, B. Chen, *et al.*, "Modulation of energy levels by donor groups: an effective approach for optimizing the efficiency of zinc-porphyrin based solar cells," *Journal of Materials Chemistry*, vol. 22, pp. 7434-7444, 2012.

[110] M. Kumar, A. Dubey, N. Adhikari, S. Venkatesan, and Q. Qiao, "Strategic review of secondary phases, defects and defect-complexes in kesterite CZTS–Se solar cells," *Energy & Environmental Science*, vol. 8, pp. 3134-3159, 2015.

[111] J. B. Li, V. Chawla, and B. M. Clemens, "Investigating the role of grain boundaries in CZTS and CZTSSe thin film solar cells with scanning probe microscopy," *Advanced Materials*, vol. 24, pp. 720-723, 2012.

[112] D. Mitzi and K. Liang, "Synthesis, resistivity, and thermal properties of the cubic perovskite NH 2 CH= NH 2 SnI 3 and related systems," *Journal of Solid State Chemistry*, vol. 134, pp. 376-381, 1997.

[113] Y. Chang, C. Park, and K. Matsuishi, "First-Principles Study of the Structural and the Electronic Properties of the Lead-Halide-Based Inorganic-Organic Perovskites (CH~ 3NH~ 3) PbX~ 3 and CsPbX~ 3 (X= Cl, Br, I)," *JOURNAL-KOREAN PHYSICAL SOCIETY*, vol. 44, pp. 889-893, 2004.

[114] R. W. RE and M. W. MA, "Alkylammonium lead halides. Part 2. CH3NH3PbX3 (X= C1, Br, I) perovskites: cuboctahedral halide cages with isotropic cation reorientation1," *Can. J. Chem.*, vol. 68, pp. 412-422, 1990.

[115] Z. Liang, S. Zhang, X. Xu, N. Wang, J. Wang, X. Wang, *et al.*, "A large grain size perovskite thin film with a dense structure for planar heterojunction solar cells via spray deposition under ambient conditions," *RSC Advances*, vol. 5, pp. 60562-60569, 2015.

[116] J. S. Yun, A. Ho-Baillie, S. Huang, S. H. Woo, Y. Heo, J. Seidel, *et al.*, "Benefit of grain boundaries in organic–inorganic halide planar perovskite solar cells," *The Journal of Physical Chemistry Letters*, vol. 6, pp. 875-880, 2015.

[117] Y. Yan, C.-S. Jiang, R. Noufi, S.-H. Wei, H. Moutinho, and M. Al-Jassim, "Electrically benign behavior of grain boundaries in polycrystalline CuInSe 2 films," *Physical review letters*, vol. 99, p. 235504, 2007.

[118] O. Douhéret, L. Lutsen, A. Swinnen, M. Breselge, K. Vandewal, L. Goris, *et al.*, "Nanoscale electrical characterization of organic photovoltaic blends by conductive atomic force microscopy," *Applied physics letters*, vol. 89, p. 032107, 2006.

[119] R. Marsh, C. McNeill, A. Abrusci, A. Campbell, and R. H. Friend, "A unified description of current–voltage characteristics in organic and hybrid photovoltaics under low light intensity," *Nano letters*, vol. 8, pp. 1393-1398, 2008.

[120] M. Dante, J. Peet, and T.-Q. Nguyen, "Nanoscale charge transport and internal structure of bulk heterojunction conjugated polymer/fullerene solar cells by scanning probe microscopy," *The Journal of Physical Chemistry C*, vol. 112, pp. 7241-7249, 2008.